

Quantum Zeno Monte Carlo for computing observables

Mancheon Han,^{1,*} Hyowon Park,^{2,3,†} and Sangkook Choi^{1,‡}

¹*School of Computational Sciences, Korea Institute for Advanced Study (KIAS), Seoul, 02455, Korea*

²*Materials Science Division, Argonne National Laboratory, Argonne, IL, 60439, USA*

³*Department of Physics, University of Illinois at Chicago, Chicago, IL, 60607, USA*

(Dated: January 7, 2025)

The recent development of logical quantum processors marks a pivotal transition from the noisy intermediate-scale quantum (NISQ) era to the fault-tolerant quantum computing (FTQC) era. These devices have the potential to address classically challenging problems with polynomial computational time using quantum properties. However, they remain susceptible to noise, necessitating noise resilient algorithms. We introduce Quantum Zeno Monte Carlo (QZMC), a classical-quantum hybrid algorithm that demonstrates resilience to device noise and Trotter errors while showing polynomial computational cost for a gapped system. QZMC computes static and dynamic properties without requiring initial state overlap or variational parameters, offering reduced quantum circuit depth.

The quantum computer [1–3] utilizes quantum algorithms to tackle computationally challenging problems, offering potential solutions to classically hard problems. A significant challenge lies in finding Hamiltonian eigenstates and their physical properties [4], crucial for material design and quantum machine learning implementation. By providing an initial state sufficiently close to the target eigenstate, this problem can be solved within polynomial quantum time [5, 6] with a fully fault-tolerant quantum computer (FTQC) [7, 8]. However, the preceding decades have been marked by the noisy intermediate-scale quantum (NISQ) era [9] rather than the FTQC era. Due to substantial device noise, quantum algorithms for NISQ systems prioritize noise resilience, leading to the dominance of ansatz-based algorithms [10, 11] without provable polynomial complexity.

The emergence of quantum devices with 48 logical qubits [12] marks the start of error-corrected quantum computing. These devices, along with their future advancements, have the potential to showcase quantum advantage, bridging the gap between NISQ and FTQC eras. Early error-corrected quantum computers are expected to handle longer quantum circuits than NISQ devices and execute quantum algorithms with polynomial complexity. However, algorithms designed for the FTQC era may not be suitable for early error-corrected quantum computers, as they still face device noise due to limited error corrections. As a result, developing new quantum algorithms that costs polynomial quantum time and are resilient to noise shows promise for achieving quantum advantage in early error-corrected quantum computers.

We introduce the quantum Zeno Monte Carlo (QZMC) algorithm. This algorithm is robust against device noise as well as Trotter error. Furthermore, this algorithm enables the computation of static as well as dynamic physical properties for gapped quantum systems within polynomial quantum time. Notably, QZMC does not necessitate overlap between the initial state and the target state, nor does it requires variational

parameters. We validate its resilience to device noise by implementing it on IBM’s NISQ devices for systems with up to 12 qubits. We also demonstrate its resilience to the Trotter error and the polynomial dependence of its computational cost by numerical demonstration on a noiseless quantum computer simulator. Our method’s resilience to Trotter errors allows us to compute eigenstate properties with shallower circuits, as demonstrated in comparisons with recent phase estimation techniques [13, 14].

RESULTS

The Quantum Zeno Monte Carlo algorithm draws inspiration from the quantum Zeno effect [15]. This is the phenomenon that repeated measurements slow down state transitions. We briefly outline this effect: A system varying with a continuous variable λ is represented by the state $|\psi_\lambda\rangle$. Increasing λ to $\lambda + \Delta\lambda$ yields the state $|\psi_{\lambda+\Delta\lambda}\rangle$, which remains $|\psi_\lambda\rangle$ with a probability of $|\langle\psi_\lambda|\psi_{\lambda+\Delta\lambda}\rangle|^2$. Because its maximum is at $\Delta\lambda = 0$, this probability becomes $1 - \mathcal{O}((\Delta\lambda)^2)$ for sufficiently small $\Delta\lambda$. By dividing $\Delta\lambda$ into N slices and measuring at each interval of $\Delta\lambda/N$, the probability of measuring $|\psi_\lambda\rangle$ is $1 - \mathcal{O}((\Delta\lambda)^2/N)$. Increasing the measurement frequency N ensures the system remains in its initial state $|\psi_\lambda\rangle$.

While the original article [15] focused on state freezing through continuous measurements, the principle can also be applied to obtain an energy eigenstate by varying the Hamiltonian for each measurement [16–20]. Let’s denote our target Hamiltonian as H , with its eigenstate as $|\Phi\rangle$. Suppose we have an easily preparable eigenstate $|\Phi_0\rangle$ of H_0 and the state is adiabatically connected to $|\Phi\rangle$. Due to the Van Vleck catastrophe [21, 22], $|\Phi_0\rangle$ has very small overlap with $|\Phi\rangle$ in general, potentially requiring a large number of measurements to obtain $|\Phi\rangle$ directly from $|\Phi_0\rangle$. Instead, we consider measuring $H_\alpha = (1 - \lambda_\alpha)H_0 + \lambda_\alpha H$ consecutively for $\lambda_\alpha = 1/N_\alpha, 2/N_\alpha, \dots, 1$. Utilizing the quantum Zeno principle, we can obtain $|\Phi\rangle$ with very high probability as we increase the number of consecutive measurements N_α .

* mchan@kias.re.kr

† hyowon@uic.edu

‡ sangkookchoi@kias.re.kr

Quantum Zeno Monte Carlo

The quantum Zeno principle can be implemented using projections, which is equivalent to measurements. Let's consider $H_\alpha = (1 - \lambda_\alpha)H_0 + \lambda_\alpha H$ with $\lambda_\alpha = 1/N_\alpha, 2/N_\alpha, \dots, 1$, and $|\Phi_0\rangle$ is the eigenstate of H_0 that can be readily prepared. For the eigenstate $|\Phi_\alpha\rangle$ of H_α , the operator that projects onto $|\Phi_\alpha\rangle$ is represented as $|\Phi_\alpha\rangle\langle\Phi_\alpha|$. Then, the consecutive projections \mathcal{P}_α applied to $|\Phi_0\rangle$ is

$$|\Psi_\alpha\rangle = \mathcal{P}_\alpha |\Phi_0\rangle, \quad \mathcal{P}_\alpha = |\Phi_\alpha\rangle\langle\Phi_\alpha| \dots |\Phi_1\rangle\langle\Phi_1|, \quad (1)$$

which is equal to $|\Phi_\alpha\rangle$ apart from the normalization. The quantum Zeno principle ensures that $\langle\Psi_\alpha|\Psi_\alpha\rangle$ approaches 1 as $N_\alpha \rightarrow \infty$. Direct implementation of $|\Phi_\alpha\rangle\langle\Phi_\alpha|$ is not straightforward, and approximating it requires knowledge of the exact eigenstate, which is unknown. To address this, we consider the projection onto the subspace with the energy E . This projection is defined as $P_H(E) = \sum_j |j\rangle\langle j| \mathbb{1}_{\mathcal{E}_j=E}$, where \mathcal{E}_j and $|j\rangle$ are the energy eigenvalues and eigenstates of the Hamiltonian H . The function $\mathbb{1}_{a=b}$ is an indicator function that equals 1 if $a = b$, and 0 otherwise. By approximating the indicator function $\mathbb{1}_{\mathcal{E}_j=E}$ with the Gaussian function $\exp(-\beta^2(\mathcal{E}_j - E)^2/2)$, we obtain the approximate projection function:

$$P_H^\beta(E) = \sum_j |j\rangle\langle j| e^{-\beta^2(\mathcal{E}_j - E)^2/2} = e^{-\beta^2(H - E)^2/2}, \quad (2)$$

which satisfies $\lim_{\beta \rightarrow \infty} P_H^\beta(E) = P_H(E)$. This non-unitary operator can not be directly implemented in the quantum computer, which only allows the unitary operation. Instead, we use a Fourier expansion [23–26] of the approximate projection,

$$P_H^\beta(E) = \frac{1}{\sqrt{2\pi\beta^2}} \int_{-\infty}^{\infty} e^{-\frac{t^2}{2\beta^2}} e^{-i(H-E)t} dt. \quad (3)$$

Here, the integrand corresponds to Hamiltonian time evolution, which can be simulated in polynomial time on a quantum computer [27, 28]. Then, the consecutive projection \mathcal{P}_α can be approximated as

$$\mathcal{P}_\alpha^\beta = P_{H_\alpha}^\beta(E_\alpha) P_{H_{\alpha-1}}^\beta(E_{\alpha-1}) \dots P_{H_1}^\beta(E_1), \quad (4)$$

where E_α is the energy eigenvalue of H_α corresponding to $|\Phi_\alpha\rangle$. By substituting \mathcal{P}_α with \mathcal{P}_α^β , the consecutive projection transforms into a multidimensional integral of consecutive time evolution. Using this expansion, we focus on computing the expectation values $\langle O \rangle$ of observables similar to recently proposed algorithms [23, 24]. Specifically, $\langle O \rangle_\alpha = \langle \Phi_\alpha | O | \Phi_\alpha \rangle$ is determined as

$$\langle O \rangle_\alpha = \frac{\langle \Psi_\alpha | O | \Psi_\alpha \rangle}{\langle \Psi_\alpha | \Psi_\alpha \rangle}, \quad (5)$$

which requires the computation of $\langle \Psi_\alpha | O | \Psi_\alpha \rangle$ and $\langle \Psi_\alpha | \Psi_\alpha \rangle$. For an operator A , $\langle \Psi_\alpha | A | \Psi_\alpha \rangle$ can be calculated by using approximating consecutive projection \mathcal{P}_α by Eq. (4). This leads

to $\langle \Psi_\alpha | A | \Psi_\alpha \rangle \approx \langle \Psi_\alpha^\beta | A | \Psi_\alpha^\beta \rangle$, where

$$\begin{aligned} \langle \Psi_\alpha^\beta | A | \Psi_\alpha^\beta \rangle &= \frac{1}{(2\pi\beta^2)^\alpha} \int dt_1 dt_2 \dots dt_{2\alpha} e^{-\frac{t_1^2 + t_2^2 + \dots + t_{2\alpha}^2}{2\beta^2}} \\ &\quad \langle \Phi_0 | e^{-iK_1 t_{2\alpha}} e^{-iK_2 t_{2\alpha-1}} \dots e^{-iK_\alpha t_{\alpha+1}} \\ &\quad A e^{-iK_\alpha t_\alpha} e^{-iK_{\alpha-1} t_{\alpha-1}} \dots e^{-iK_1 t_1} | \Phi_0 \rangle. \end{aligned} \quad (6)$$

where $K_{\alpha'}$ is equal to $H_{\alpha'} - E_{\alpha'}$ for $\alpha' = 1, 2, \dots, \alpha$. This integral can be evaluated using the Monte Carlo method [29] by sampling $t_1, t_2, \dots, t_{2\alpha}$ from a Gaussian distribution. More precisely,

$$\begin{aligned} \langle \Psi_\alpha^\beta | A | \Psi_\alpha^\beta \rangle &= \frac{1}{N_\nu} \sum_{\mathbf{t}_\nu} \langle \Phi_0 | e^{-iK_1 t_{\nu,2\alpha}} e^{-iK_2 t_{\nu,2\alpha-1}} \dots \\ &\quad e^{-iK_\alpha t_{\nu,\alpha+1}} A e^{-iK_\alpha t_{\nu,\alpha}} e^{-iK_{\alpha-1} t_{\nu,\alpha-1}} \dots e^{-iK_1 t_{\nu,1}} | \Phi_0 \rangle, \end{aligned} \quad (7)$$

where N_ν is the number of samples of $\mathbf{t}_\nu = [t_{\nu,1} \ t_{\nu,2} \ \dots \ t_{\nu,2\alpha}]^T$. Each $t_{\nu,k}$ is drawn from a Gaussian distribution with a standard deviation of β . We refer to this approach as the quantum Zeno Monte Carlo (QZMC) method. From its formulation, it is evident that QZMC can be used to compute various static and dynamic properties of Hamiltonian eigenstates. Figure 1 provides a summary of the method.

Among various eigenstate properties, the energy eigenvalue holds prime importance, as it is essential for QZMC to perform the approximate projection $P_H(E)$. In this section, we describe the method for computing energy eigenvalues using Quantum Zeno Monte Carlo. QZMC employs eigenstates $|\Psi_\alpha\rangle$, which satisfy $\langle \Psi_\alpha | \Phi_\alpha \rangle \langle \Phi_\alpha | (H_\alpha - H_{\alpha-1}) | \Psi_{\alpha-1} \rangle = (E_\alpha - E_{\alpha-1}) \langle \Psi_\alpha | \Psi_\alpha \rangle$. Using this, the energy eigenvalue is estimated from

$$E_\alpha = E_{\alpha-1} + \frac{\langle \Psi_\alpha | \Phi_\alpha \rangle \langle \Phi_\alpha | (H_\alpha - H_{\alpha-1}) | \Psi_{\alpha-1} \rangle}{\langle \Psi_\alpha | \Psi_\alpha \rangle}. \quad (8)$$

This equation can be computed using the same strategy we used in Eq. (7). Compared to estimating entire energy from $\langle H_\alpha \rangle_\alpha$ using Eq. (5), this approach improves robustness against noise by limiting its impact to the energy difference alone. Building on this insight, we propose the predictor-corrector QZMC method for determining energy eigenvalues. Suppose we know $E_0, E_1, \dots, E_{\alpha-1}$ and seek to compute E_α . Inspired by the predictor-corrector method commonly used for solving differential equations [30], we begin with an initial estimate of E_α , referred to as the predictor. Various approaches can be employed to determine the predictor. One frequently used method in this manuscript is the first-order perturbation approximation [31], given by $E_\alpha = E_{\alpha-1} + \langle \Phi_{\alpha-1} | (H_\alpha - H_{\alpha-1}) | \Phi_{\alpha-1} \rangle$. Here, $\langle \Phi_{\alpha-1} | (H_\alpha - H_{\alpha-1}) | \Phi_{\alpha-1} \rangle$ is computed using Eq. (5). Using the predictor E_α , we then compute a more accurate estimate of E_α using Eq. (8). Further details of the QZMC method, including formulations for the computation of Green's functions, are provided in the Supplementary Information Sec. I.

In the formulation of the method, we began with H_0 , which can be easily solved on a classical computer, and whose eigenstate $|\Phi_0\rangle$ is readily preparable as a quantum circuit. Notably, $|\Phi_0\rangle$ is not required to have a finite overlap with the target eigenstate $|\Phi\rangle$. However, the synthesis of arbitrary unitary operations can incur exponential quantum time costs [32], making the preparation of $|\Phi_0\rangle$ challenging even when H_0 is exactly solvable on a classical computer. Our method can also be applied in such cases by following an alternative procedure. First, we prepare an easily accessible state $|\tilde{\Phi}_0\rangle$ with a finite overlap with $|\Phi_0\rangle$ (e.g., $|\langle\Phi_0|\tilde{\Phi}_0\rangle|^2 > 0.5$). Then, we project $|\tilde{\Phi}_0\rangle$ onto $|\Phi_0\rangle$ using Eq. (2) and perform QZMC in an equivalent way. Consequently,

$$|\Psi_\alpha\rangle = \mathcal{P}_\alpha |\Phi_0\rangle \langle\Phi_0|\tilde{\Phi}_0\rangle, \quad (9)$$

is used instead of Eq. (1). As $|\Phi_0\rangle$ is known and can be processed on a classical computer, finding $|\tilde{\Phi}_0\rangle$ can be efficiently accomplished using classical computing resources. Thus, applying QZMC is feasible even for systems where $|\Phi_0\rangle$ is not easily preparable

Finally, we note that the transformation in Eq. (3) can be interpreted as the Hubbard-Stratonovich transformation [33–35], which underpins the auxiliary-field quantum Monte Carlo (AFQMC) method [36, 37]. AFQMC is a widely-used classical approach for computing ground state properties of quantum many-body systems. In AFQMC, the Hubbard-Stratonovich transformation is employed to transform two-body interactions term into one-body term at the cost of introducing auxiliary fields. In contrast, QZMC leverages a similar transformation to express non-unitary operators as integrals over unitary operations, enabling its implementation on quantum computers. Unlike AFQMC or diffusion Monte Carlo (DMC) [38], which iteratively adjust the trial energy as random walkers propagate in imaginary time under a fixed Hamiltonian, QZMC calculates the ground-state energy by integrating the energy difference formula (Eq. (8)) while gradually changing the Hamiltonian toward the target Hamiltonian.

Error analysis and Cost estimation

This section provides an error analysis and cost estimation for our method. A detailed analysis is available in Sec. II of the Supplementary Information. For simplicity, we assume a linear interpolation between H_0 and H , defined as $H_\alpha = H_0 + \lambda_\alpha H'$, where $H' = H - H_0$ and $\lambda_\alpha = 1/N_\alpha, 2/N_\alpha, \dots, 1$. We also assume the target state is gapped from other states, with a lower bound Δ_g on the energy gap. The computational cost is evaluated in terms of circuit depth and the number of circuits (N_ν) required. Circuit depth depends on N_α and systematic errors from β , while the number of circuits accounts for statistical errors arising from Gaussian sampling of t_ν . The goal is to estimate the energy eigenvalue within an error ϵ . From the formulation (e.g., Eq. (5), (8)), it is essential to maintain a finite value of $\langle\Psi_\alpha^\beta|\Psi_\alpha^\beta\rangle$ for a feasible computation. We first analyze error of $\langle\Psi_\alpha^\beta|\Psi_\alpha^\beta\rangle$ and address the condition under which $\langle\Psi_\alpha^\beta|\Psi_\alpha^\beta\rangle \geq (1 - \eta)$ for $\eta \in (0, 1)$.

Error analysis of $\langle\Psi_\alpha^\beta|\Psi_\alpha^\beta\rangle$

Our analysis begins with the assumption of exact projection. We then incorporate the effects of finite β , trotterization, and N_ν . We decompose η as $\eta_0 + \delta\eta_\beta + \delta\eta_T + \delta\eta_{\text{mc}}$, where η_0 corresponds to exact projection, $\delta\eta_\beta$ represents the error due to finite β , $\delta\eta_T$ arises from trotterization, and $\delta\eta_{\text{mc}}$ reflects the finite number of samplings.

First, under the assumption of exact projection, we estimate the number of projections N_α required to satisfy $\langle\Psi_\alpha|\Psi_\alpha\rangle \geq 1 - \eta_0$. Applying perturbation theory [31], we obtain

$$|\langle\Phi_\alpha|\Phi_{\alpha+1}\rangle|^2 \geq 1 - \|H'\|^2 \Delta_g^{-2} N_\alpha^{-2} \quad (10)$$

up to the leading order in N_α^{-1} . Consequently, $\langle\Psi_\alpha|\Psi_\alpha\rangle = |\langle\Phi_0|\Phi_1\rangle|^2 |\langle\Phi_1|\Phi_2\rangle|^2 \dots |\langle\Phi_{\alpha-1}|\Phi_\alpha\rangle|^2$ is bounded below by $1 - \|H'\|^2 / \Delta_g^{-2} N_\alpha^{-1}$. By setting $N_\alpha \geq \|H'\|^2 \Delta_g^{-2} \eta_0^{-1}$, we ensure that $\langle\Psi_\alpha|\Psi_\alpha\rangle \geq 1 - \eta_0$. For the ground state, a smaller N_α can be used due to the ground state property, yielding

$$N_\alpha \geq \|H'\| \Delta_g^{-1} \eta_0^{-1}. \quad (11)$$

Please see Sec. II A 1 of Supplementary Information for derivations of Eq. (10) and Eq. (11).

Next, we examine the effect of finite β . The error in the projected state due to finite β can be written as $|\delta\Psi_\alpha^\beta\rangle = |\Psi_\alpha^\beta\rangle - |\Psi_\alpha\rangle$. Perturbative analysis shows that

$$\|\delta\Psi_\alpha^\beta\| \leq (\alpha/N_\alpha) e^{-\beta^2 \Delta_g^2 / 2} \|H'\| \Delta_g^{-1}, \quad (12)$$

up to the leading order in $1/N_\alpha$. As a result, $\delta\eta_\beta \leq 2 \exp(-\beta^2 \Delta_g^2 / 2) \|H'\| \Delta_g^{-1}$. By choosing

$$\beta \geq \Delta_g^{-1} \sqrt{2} \log^{1/2}(2 \|H'\| \Delta_g^{-1} (\eta - \eta_0)^{-1}), \quad (13)$$

we ensure that $\eta_0 + \delta\eta_\beta \leq \eta$.

For time evolution, we primarily use trotterization. The circuit depth required for our method is determined by the total number of trotterization steps. The error in the projected state due to trotterization is expressed as $|\delta\Psi_\alpha^{\beta,T}\rangle = |\Psi_\alpha^{\beta,T}\rangle - |\Psi_\alpha^\beta\rangle$, where $|\delta\Psi_\alpha^{\beta,T}\rangle$ rises from trotterized time evolutions. The trotterization error for each α -th time evolution with evolution time t is bounded by $C_{\alpha,p} |t|^{1+p} N_{T,\alpha}^{-p}$, where $N_{T,\alpha}$ is the number of trotterization steps for each α , p is the trotterization order, and $C_{\alpha,p}$ is the coefficient which is proportional to the sum of the norms of the commutators [39]. Then, we can show

$$\|\delta\Psi_\alpha^{\beta,T}\| \leq \sum_{\alpha'=1}^{\alpha} C_{\alpha',p} M_{1+p}(\beta) N_{T,\alpha'}^{-p}, \quad (14)$$

and $\delta\eta_T \leq 2 \sum_{\alpha'=1}^{N_\alpha} C_{\alpha',p} M_{1+p}(\beta) N_{T,\alpha'}^{-p}$, up to the leading order of $N_{T,\alpha}^{-1}$. Here $M_{1+p}(\beta)$ is the expectation value of $|t|^{1+p}$ for a Gaussian distribution with a standard deviation of β . To ensure the trotterization error is smaller than $\delta\eta_T$, the total number of trotter steps $N_T = 2 \sum_{\alpha=1}^{N_\alpha} N_{T,\alpha}$ can be chosen as

$$N_T \geq 2 \left(\frac{2N_\alpha}{\delta\eta_T} \right)^{1/p} \sum_{\alpha=1}^{N_\alpha} C_{\alpha,p}^{1/p} M_{1+p}^{1/p}(\beta), \quad (15)$$

with each $N_{T,\alpha}$ proportional to $C_{\alpha,p}^{1/p} M_{1+p}^{1/p}(\beta)$.

Finally, we consider the statistical error $\delta\eta_{mc}$, which arises from the finite number of samples N_ν . Defining $x(\mathbf{t}) = \langle \Phi_0 | e^{-iK_1 t_{2\alpha}} e^{-iK_2 t_{2\alpha-1}} \dots e^{-iK_\alpha t_{\alpha+1}} A e^{-iK_\alpha t_\alpha} e^{-iK_{\alpha-1} t_{\alpha-1}} \dots e^{-iK_1 t_1} | \Phi_0 \rangle$, $g(\mathbf{t}) = (2\pi\beta^2)^{-\alpha} e^{-(t_1^2+t_2^2+\dots+t_{2\alpha}^2)/(2\beta^2)}$, Eq. (6) can be seen as finding the expectation value $E[x]$ of $x(\mathbf{t})$ with the probability of $g(\mathbf{t})$. The case of $A = \mathbb{I}$ corresponds to $\langle \Psi_\alpha^\beta | \Psi_\alpha^\beta \rangle$. The variance of x , σ_x^2 , is given by $E[x^2] - (E[x])^2$. Since $\|x(\mathbf{t})\| \leq 1$, $\sigma_x^2 \leq 1 - (E[x])^2$. So, the standard error of $\langle \Psi_\alpha^\beta | \Psi_\alpha^\beta \rangle$ using N_ν samples is bounded by $N_\nu^{-1/2}(2\eta - \eta^2)$. Therefore, getting $\langle \Psi_\alpha^\beta | \Psi_\alpha^\beta \rangle$ with desired precision $\delta\eta_{mc}$ will require

$$N_\nu \geq (2\eta - \eta)^2 \delta\eta_{mc}^{-2}. \quad (16)$$

In the sampling procedure, an additional source of statistical error, known as shot noise, arises. On currently accessible quantum computers, each circuit is measured with N_s repeated measurements, referred to as ‘‘shots’’. The finite number of shots introduces a standard error of $1/\sqrt{N_s}$ for each measurement. This modified the statistical error dependence from $N_\nu^{-1/2}$ to $N_\nu^{-1/2}(1 + N_s^{-1/2})$.

Error analysis of E_α

The error ϵ of E_α is analyzed similarly to $\langle \Psi_\alpha^\beta | \Psi_\alpha^\beta \rangle$. Like η , ϵ is decomposed as $\epsilon_\beta + \epsilon_T + \epsilon_{mc}$. Here, ϵ_β arises from the finite β , ϵ_T is due to trotterization, and ϵ_{mc} results from the finite number of samples.

First, we consider the energy estimation error arises from finite β , ϵ_β . In our method, the energy difference is computed based on Eq. (8). Each energy difference estimator introduces an error of order $N_\alpha^{-1} \|H'\| \| |\delta\Psi_{\alpha-1}^\beta\rangle \| / (1 - \eta)$. Detailed calculations in Sec. II B 1 of the Supplementary Information show that the proportionality constant is 4. Thus $\epsilon_\beta \leq \sum_{\alpha=1}^{N_\alpha} 4N_\alpha^{-1} \| |\delta\Psi_{\alpha-1}^\beta\rangle \| \|H'\| / (1 - \eta)$. From Eq. (12), we have

$$\epsilon_\beta \leq 2 \exp(-\beta^2 \Delta_g^2 / 2) \|H'\|^2 \Delta_g^{-1} / (1 - \eta) \quad (17)$$

To ensure the projection error is smaller than ϵ_β , we use β that satisfy

$$\beta \geq \Delta_g^{-1} \sqrt{2} \log^{1/2}(2 \|H'\|^2 \Delta_g^{-1} (1 - \eta)^{-1} \epsilon_\beta^{-1}). \quad (18)$$

The discussion of the trotterization error follows a similar approach to that of β . The error ϵ_T is bounded as $\epsilon_T \leq \sum_{\alpha=1}^{N_\alpha} 4N_\alpha^{-1} \| |\delta\Psi_{\alpha-1}^{\beta,T}\rangle \| \|H'\| / (1 - \eta)$. Using Eq. (14) and assuming $N_{T,\alpha}$ is determine to be proportional to $C_{\alpha,p}^{1/p} M_{1+p}^{1/p}(\beta)$, the error can be expressed as

$$\epsilon_T \leq 2N_\alpha \left(\frac{N_T}{2} \right)^{-p} \left(\sum_{\alpha=1}^{N_\alpha} C_{\alpha,p}^{1/p} M_{1+p}^{1/p}(\beta) \right)^p \frac{\|H'\|}{1 - \eta}. \quad (19)$$

To achieve a desired ϵ_T , the total number of trotter steps can be chosen as

$$N_T \geq 2 \frac{(2N_\alpha \|H'\|)^{1/p}}{(\epsilon_T(1 - \eta))^{1/p}} \sum_{\alpha=1}^{N_\alpha} C_{\alpha,p}^{1/p} M_{1+p}^{1/p}(\beta). \quad (20)$$

In practice, Trotter errors are considerably smaller than the theoretical bounds [39, 40]. Additionally, as discussed in [Noise resilience of QZMC](#) section, error cancellation occurs between the numerator and the denominator. Consequently, the number of Trotter steps required is substantially lower than the theoretical estimate.

To estimate the statistical error ϵ_{mc} in the energy calculation, we examine Eq. (8). The numerator in this equation is computed through a Monte Carlo summation of $\langle \Phi_0 | e^{-iK_1 t_{\nu,2\alpha}} e^{-iK_2 t_{\nu,2\alpha-1}} \dots e^{-iK_\alpha t_{\nu,\alpha+1}} e^{-iK_\alpha t_{\nu,\alpha}} \Delta\lambda H' e^{-iK_{\alpha-1} t_{\nu,\alpha-1}} e^{-iK_{\alpha-2} t_{\nu,\alpha-2}} \dots e^{-iK_1 t_{\nu,1}} | \Phi_0 \rangle$. Because time evolutions are unitary, each term in the summation is bounded by $\Delta\lambda \|H'\|$. This results in a Monte Carlo error of the numerator bounded by $\Delta\lambda \|H'\| / \sqrt{N_\nu}$. Taking into account the effect of the denominator and summing over α from 1 to N_α , we find that the total error is bounded by

$$\epsilon_{mc} \leq \|H'\| / \sqrt{N_\nu} (1 - \eta)^{-1} (1 + (1 - \eta)^2)^{-1/2}. \quad (21)$$

The statistical precision of ϵ_{mc} can be achieved by using N_ν such that

$$N_\nu \geq \epsilon_{mc}^{-2} \|H'\|^2 (1 - \eta)^{-2} (1 + (1 - \eta)^2). \quad (22)$$

Computational cost

Based on the error analysis discussed, we estimate the computational cost of determining the ground state energy using QZMC and summarize the results in Table I.

First, we discuss the circuit depth required to estimate ground state energy using QZMC. Excluding the cost of preparing the initial state, the circuit depth required for our method is determined by the total time evolution length, which is proportional to βN_α . From the previous discussion, $N_\alpha \propto \Delta_g^{-1} \|H'\|$, so $N_\alpha = \mathcal{O}(\Delta_g^{-1} \text{poly}(n))$. Similarly, $\beta \propto \Delta_g^{-1} (\log(2 \|H'\| \Delta_g^{-1} (1 - \eta)^{-1} \epsilon^{-1}))^{1/2}$, $\beta = \mathcal{O}(\Delta_g^{-1} \log^{1/2}(\Delta_g^{-1} \epsilon^{-1} n))$. Therefore, the total time evolution length required for our method is $\mathcal{O}(\Delta_g^{-2} \log^{1/2}(\Delta_g^{-1} \epsilon^{-1} n) \text{poly}(n))$.

The practical implementation of our method requires trotterization, so the circuit depth for QZMC is determined by the total number of Trotter steps N_T . From the previous discussion, $N_T \propto \epsilon^{-1/p} \|H'\|^{1/p} N_\alpha^{1/p} (\sum_{\alpha} C_{\alpha,p}^{1/p} M_{1+p}^{1/p}(\beta))$, where p is the order of trotterization. Since $C_{\alpha,p} = \mathcal{O}(\text{poly}(n))$ [39] and $M_{1+p}^{1/p}(\beta) = \mathcal{O}(\beta^{(1+1/p)})$, $N_T = \mathcal{O}(\epsilon^{-1/p} \text{poly}(n) (\beta N_\alpha)^{1+1/p})$. Substituting β and N_α , we have

$$N_T = \mathcal{O}(\epsilon^{-\frac{1}{p}} \Delta_g^{-2-\frac{2}{p}} \log^{\frac{1}{2}+\frac{1}{2p}}(\Delta_g^{-1} \epsilon^{-1} n) \text{poly}(n)). \quad (23)$$

Second, we discuss the total number of samples required to estimate ground state energy within a precision of ϵ . From Eq. (22), the number of samples N_ν required to achieve a precision ϵ is $\mathcal{O}(\epsilon^{-2} \text{poly}(n))$. Since QZMC should be performed for $\alpha = 1, 2, \dots, N_\alpha$, the total number of samples required is $\mathcal{O}(\epsilon^{-2} \text{poly}(n)N_\alpha) = \mathcal{O}(\Delta_g^{-1} \epsilon^{-2} \text{poly}(n))$.

Remarks

A key characteristic of our method is that the approximate projection depends on the energy estimate ϵ , meaning the calculational precision can affect subsequent calculations. If ϵ comparable to or larger than Δ_g , the approximate projection fails to target the desired states, making the calculations infeasible. For ϵ much smaller than Δ_g , the projected state becomes $\exp(-\alpha\beta^2\epsilon^2/2)|\Psi_\alpha^\beta\rangle$, inducing attenuation of $r_\alpha = \exp(-N_\alpha\beta^2\epsilon^2)$ of $\langle\Psi_\alpha^\beta|\Psi_\alpha^\beta\rangle$ for $\alpha = N_\alpha$. To ensure $r_\alpha \geq r$ for some finite r , β should satisfy $\beta \leq \epsilon^{-1}N_\alpha^{-1/2} \log^{-1/2}(1/r)$. Thus the energy estimate precision ϵ imposes a limit on β .

Another aspect worth addressing is the potential for a sign problem. The error analysis and computational cost estimation indicate that our method is, in principle, free from the sign problem for gapped systems. For such systems, for any $\eta \in (0, 1)$, there exist sufficiently large parameters β , N_α , and N_ν , scaling polynomially with the number of qubits n , such that $\langle\Psi_\alpha^\beta|\Psi_\alpha^\beta\rangle$ is lower-bounded by $1 - \eta$. In practice, error sources such as Trotter errors and device noise reduce $\langle\Psi_\alpha^\beta|\Psi_\alpha^\beta\rangle$, resulting in noise amplification in Eq. (5) and Eq. (8), analogous to the conventional sign problem in Monte Carlo methods.

The realization of our method requires computing the overlap between the initial and time-evolved states on a quantum computer. In the most general setting, this involves controlled time evolution [3], which demands attaching control lines to every gate, making it resource-intensive. However, if H_α shares a common eigenstate, controlled time evolution can be avoided, as shown in other methods [14]. Since chemical and physical Hamiltonians often share a common eigenstate, such as the vacuum, this feature makes our method practical for applications in chemistry and physics. For the specific form of the quantum circuit used in our method, see Sec. IID 2 of the Supplementary Information.

Applications of QZMC

Here, we verify our method by applying it to solve various quantum many body systems.

First, we used our method to compute physical properties with NISQ devices. The first system we consider (Figure 2) is the one-qubit system with the Hamiltonian. $H(\lambda) = X/2 + (2\lambda - 1)Z$. Next, we simulate the H_2 molecule (Figure 3 (a)) in the STO-3G basis [45], a typical testbed for quantum algorithms [46, 47]. By constraining the electron number to be 2 and the total spin to be 0 [48, 49], the system can be represented by a 2-qubit Hamiltonian. We calculate the energy

spectrum of 4 low-lying eigenstates of H_2 as a function of interatomic distance (R). Then, we consider the 2-site Hubbard model [50], the Hubbard dimer. The Hubbard dimer (Figure 3 (b)-(f)) at its half filling and singlet spin configuration can also be mapped to a two-qubit Hamiltonian. 4 low-lying Energy eigenvalues of the Hubbard dimer are computed by increasing onsite Coulomb interaction (U) from 0. For these calculations, we create a discrete path with $N_\alpha = 10$, and apply the predictor-corrector QZMC for $H_\alpha = H(\lambda_\alpha)$. Lastly, we applied our method to the XXZ model (Figure 4) in one-dimension, which has the Hamiltonian

$$H = -J \sum_{i=1}^{n-1} (S_i^x S_{i+1}^x + S_i^y S_{i+1}^y + \Delta S_i^z S_{i+1}^z). \quad (24)$$

We computed systems with $n = 4$ to $n = 12$, using $J = 1$ and $\Delta = -1$. For a quantum circuit implementation of trotterization for XXZ model, we used recently suggested optimized circuit [51], with two trotter steps.

The one-qubit system results are displayed in Fig. 2. Fig. 2 (a) shows the ground and the excited state energy eigenvalues, while Fig. 2 (b) shows ground state expectation value of X , Y and Z operators. Despite device noises in *ibmq_lima*, measured observables match well with exact values (dashed lines). Moreover, computed ground state fidelity $\mathcal{F}_\alpha = |\langle\Phi_\alpha|\Psi_\alpha\rangle|^2 / \langle\Psi_\alpha|\Psi_\alpha\rangle$ (Fig. 2 (c)) is almost 1, which demonstrates accurate projection to the desired state by QZMC.

Figure 3 presents computational results for two-qubit systems: H_2 and the Hubbard dimer. We determined the energy eigenvalues of H_2 within an error of 0.02 Ha using *ibmq_lagos*. Energy eigenvalues for the Hubbard dimer are calculated within an error of $0.06t$ on *ibmq_perth*, where t is electron hopping between two hubbard atoms. And we compute the electronic spectral function $A(\omega)$ [52] of the Hubbard dimer with the NISQ device. Figure 3 (e)-(f) displays $A(\omega)$ at $k = 0$ and $k = \pi$, showing good agreements between exact values and measured values.

The additional computations for these one- and two-qubit systems, specifically the parameter dependence of QZMC for the one-qubit system and the ground state energy calculation of the Hubbard dimer with Trotterized time evolution, are provided in Sec. III of the Supplementary Information.

Figure 4 presents the computational results for the XXZ model with 4 to 12 qubits. The energy eigenvalues are well reproduced, even for 12 qubits, despite severe degradation of $\langle\Psi|\Psi\rangle$ due to device noise and trotterization errors. Specifically, we obtained ground state energy errors of 0.015 for 4 qubits, 0.0275 for 6 qubits, 0.016 for 8 qubits, 0.041 for 10 qubits, and 0.051 for 12 qubits on *ibmq_torino*. These values are significantly lower than the errors in $\langle\Psi|\Psi\rangle$ (represented by the differences between the squares and crosses) shown in the right panel of the figure. Thus, we conclude that our method provides reasonable results even in the presence of both device noise and trotterization errors. All calculations were performed with dynamical decoupling (DD) [53] and readout error mitigation [54], without employing advanced techniques such as zero-noise extrapolation (ZNE) [55–57] or

probabilistic error cancellation (PEC) [54, 58]. We anticipate that larger-scale simulations will become feasible soon with these methods or with advancements in hardware.

Next, we demonstrate our method for a large system by applying QZMC on the Hubbard model at the half-filling in various sizes with noiseless qsim-cirq [59] quantum computer simulator. As H_0 , we choose dimer array, featuring easily implementable non-degenerate ground state. We gradually increased the inter-dimer hopping t_{inter} from 0 to the desired value t as α increased. We explored two geometries, chains and ladders, with periodic boundary conditions, as illustrated in Figure 5 (a). For each geometry, we computed systems with 6, 8, and 10 sites when $U/t = 5$. For QZMC, we used $\beta = 3$, with N_α equal to the number of sites and N_ν increases as $\|H'\|^2$ increases. For the time evolution, we used the first order Trotterization [27, 39, 60], adjusting the Trotter steps as system changes. More specifically, we used a maximum of 528 Trotter steps for the 6×1 system and up to 1960 steps for the 2×5 Hubbard model.

Fig. 5 (c) shows that QZMC accurately reproduces the exact ground state energy across various configurations, from 6 to 10 sites, in both chain and ladder geometries. And our method also accurately computes local spectral function for Hubbard models as shown in in Fig. 5 (d)-(g), which reproduces the exact positions and widths of every peak in the spectral functions. Further data not included in Fig.5(c), such as $\langle \Psi | \Psi \rangle$ for all geometries and spectral functions for the 6-site Hubbard models, can be found in Sec. V of the Supplementary Information.

Finally, we computed Hubbard chains under open boundary conditions to compare our method with other methods for ground state energy estimation. We compare our method with two state-of-the-art approaches: the Heisenberg-limited method developed by Lin and Tong [14], and the quantum complex exponential least squares (QCELS) method developed by Ding and Lin [13]. We considered three cases: $4 \times 1, U = 4$; $4 \times 1, U = 10$; and $8 \times 1, U = 10$. The initial state $|\tilde{\Phi}_0\rangle$ was chosen such that $|\langle \tilde{\Phi} | \tilde{\Phi}_0 \rangle|^2 = 0.4$, matching the conditions in the references [13, 14]. Both methods were implemented as described in the respective references.

The top panels of Figure 6 compares the energy estimation error ϵ as a function of the maximum time evolution length T . In most of cases, QZMC requires a shorter T than Lin and Tong's method and is comparable to QCELS for a precision range of 10^{-4} to 10^{-2} .

The middle panels shows ϵ as a function of the total Trotterization steps N_T , which is directly proportional to the circuit depth. In these and the bottom panels, the maximum time evolution length T for each method was set to achieve a similar accuracy of about 0.003 for the exact time evolution. QZMC demonstrates higher precision with fewer Trotterization steps. For example, in the $4 \times 1, U/t = 10$ case with $N_T = 412$, the error for QZMC is 0.0046, compared to 0.043 for QCELS and 0.015 for Lin and Tong's method.

The bottom panels plots the total number of samples required for each method. Lin and Tong's method converges quickly, while QCELS and QZMC converge more slowly, with QZMC requiring the most samples, eventually reaching

approximately 10^5 .

In conclusion, overall our method achieves higher precision with shorter circuit depth compared to other state-of-the-art methods, at the cost of requiring more samples. Therefore, QZMC is particularly useful when quantum circuit depth is a limiting factor, but the number of accessible samples is not severely constrained.

In addition to the methods discussed above, our approach can also be compared to adiabatic state preparation (ASP), as both methods follow an adiabatic path. However, QZMC offers two notable advantages over ASP. First, QZMC is resilient to errors such as Trotter errors and device noise, making it more practical in scenarios where such errors are significant. Second, as highlighted in Quantum Zeno Monte Carlo section, QZMC does not require the initial state $|\Phi_0\rangle$ to be exact, whereas ASP must begin with an exact $|\Phi_0\rangle$. This distinction is important because preparing an arbitrary state on a quantum computer can be exponentially hard [32], and the flexibility to start with an approximate initial state enhances the practicality of QZMC. A comparison of ASP and QZMC under the influence of Trotter errors is presented in Sec. V of the Supplementary Information.

Noise resilience of QZMC

Interestingly, our calculational results for observables accurately reproduce exact values even with the device noises (Fig. 2 and Fig. 3) and the Trotter errors (Fig. 5). The effect of these noises induces significant deviations of calculated $\langle \Psi | \Psi \rangle$ (Fig. 2 (d), Fig. 3 (c), and Fig. 5 (b)) from exact values. However, the observable expectation values, which is computed by using the ratio of $\langle \Psi | O | \Psi \rangle$ and $\langle \Psi | \Psi \rangle$ (Eq. (5)) is robust against device noises and Trotter errors. To understand this, we tested the dependence of the calculated observables on the device noise magnitude using the qiskit [61] aer simulator. We considered $\langle \Psi | \Psi \rangle$, $\langle \Psi | Z | \Psi \rangle$, and $\langle Z \rangle$ of the ground state of the one-qubit system. Figure. 7 shows calculational results. As the noise level increases, $\langle \Psi | \Psi \rangle$ decreases and the absolute value of $\langle \Psi | Z | \Psi \rangle$ also decreases (Fig. 7 (a)). Surprisingly, these noise-induced errors cancel each other through the ratio of $\langle \Psi | \Psi \rangle$ and $\langle \Psi | Z | \Psi \rangle$, so that $\langle Z \rangle = \langle \Psi | Z | \Psi \rangle / \langle \Psi | \Psi \rangle$ (Fig. 7 (b)) remains robust against noise. Since quantum circuits for computing the numerator and denominator are nearly identical, division cancels out common noise effects, making the expectation value resilient. The same argument can be applied to Trotterization (thus, the method is resilient to Trotter error too). Because we use same Trotterization rule for both the numerator and the denominator, common Trotterization errors are canceled out by division. This have been demonstrated numerically in Fig. 8 (a)-(b). In this figure, we computed same quantities considered in Fig. 7 using trotterized time evolutions varying the total trotterization steps N_T . We can see that the low-trotterization steps makes $\langle \Psi | \Psi \rangle$ small, but $\langle Z \rangle$ does not change a lot because the magnitude of $\langle \Psi | Z | \Psi \rangle$ also decreased by the trotterization.

Figure 7 and 8 (a)-(b) demonstrate that error cancellation through division occurs in practice for both device noise and

Trotter errors. However, since these errors arise from fundamentally different sources, the mechanisms behind their cancellation differ. In followings, we provide a detailed analysis of how error cancellation occurs for each type of error and additional notes.

First, we discuss the mechanism for the device noise resilience. In our method, we measure consecutive time evolution using a single ancilla qubit (See Sec. IID 2 of the Supplementary Information for quantum circuits). With this in mind, let's examine the following simple example. Consider a qubit with the density matrix ρ . Then, exact outcome of a Z measurement on this qubit is given by $\text{Tr}(\rho Z)$. The effect of noise the qubit can be described as $\mathcal{E}(\rho)$ [3]. With this noise, the outcome of the Z measurement becomes $\text{Tr}(\mathcal{E}(\rho)Z)$. Consider the depolarizing channel as a specific type of noise, which alters the state ρ to $\mathcal{E}(\rho) = pI/2 + (1-p)\rho$. Here, p represents the probability of depolarization. With this model, $\text{Tr}(\mathcal{E}(\rho)Z)$ becomes $(1-p)\text{Tr}(\rho Z)$. Now, imagine another qubit with the density matrix ρ' subjected to the same noise channel. The Z measurement of this qubit yields $(1-p)\text{Tr}(\rho'Z)$. Then, the ratio of the measurement outcomes of two qubits with noise channel is

$$\frac{\text{Tr}(\mathcal{E}(\rho')Z)}{\text{Tr}(\mathcal{E}(\rho)Z)} = \frac{(1-p)\text{Tr}(\rho'Z)}{(1-p)\text{Tr}(\rho Z)} = \frac{\text{Tr}(\rho'Z)}{\text{Tr}(\rho Z)}, \quad (25)$$

which is same with the exact value. This demonstrates that the effect noise can be effectively canceled out by the division. Though we only showed the case with the depolarizing channel, same cancellation occurs for bit and phase flip channels. Similar discussion can also be found in the literature on the quantum-classical hybrid Quantum Monte Carlo algorithm (QC-QMC) [66], which estimates the wave function overlap efficiently using shadow tomography.

To analyze the resilience of QZMC to Trotter errors, we consider the state

$$|\Psi_{\alpha}^{\beta,T}\rangle = |\Psi_{\alpha}^{\beta}\rangle + |\delta\Psi_{\alpha}^{\beta,T}\rangle \quad (26)$$

as defined in [Error analysis of \$\langle\Psi_{\alpha}^{\beta}|\Psi_{\alpha}^{\beta}\rangle\$](#) section. The error term $|\delta\Psi_{\alpha}^{\beta,T}\rangle$ can be decomposed into two components: one parallel to $|\Psi_{\alpha}^{\beta}\rangle$ and the other orthogonal to it. Suppose the error consists only of the parallel component. In this case, we can express the state as

$$|\Psi_{\alpha}^{\beta,T}\rangle = (1 - \eta_{\parallel}/\|\Psi_{\alpha}^{\beta}\|)e^{i\phi_{\parallel}}|\Psi_{\alpha}^{\beta}\rangle. \quad (27)$$

Here, η_{\parallel} represents the norm of the parallel error, and ϕ_{\parallel} is the associated phase shift. In such a scenario, the expectation value of an observable O is

$$\begin{aligned} \frac{\langle\Psi_{\alpha}^{\beta,T}|O|\Psi_{\alpha}^{\beta,T}\rangle}{\langle\Psi_{\alpha}^{\beta,T}|\Psi_{\alpha}^{\beta,T}\rangle} &= \frac{(1 - \eta_{\parallel}/\|\Psi_{\alpha}^{\beta}\|)^2 \langle\Psi_{\alpha}^{\beta}|O|\Psi_{\alpha}^{\beta}\rangle}{(1 - \eta_{\parallel}/\|\Psi_{\alpha}^{\beta}\|)^2 \langle\Psi_{\alpha}^{\beta}|\Psi_{\alpha}^{\beta}\rangle} \\ &= \frac{\langle\Psi_{\alpha}^{\beta}|O|\Psi_{\alpha}^{\beta}\rangle}{\langle\Psi_{\alpha}^{\beta}|\Psi_{\alpha}^{\beta}\rangle}. \end{aligned} \quad (28)$$

Thus, the parallel component of the error cancels out through division, demonstrating that QZMC is inherently resilient to this type of Trotter error.

In practice, however, the error also contains an orthogonal component $\eta_{\perp}|\Psi_{\alpha,\perp}^{\beta}\rangle$, resulting in

$$|\Psi_{\alpha}^{\beta,T}\rangle = (1 - \eta_{\parallel}/\|\Psi_{\alpha}^{\beta}\|)e^{i\phi_{\parallel}}|\Psi_{\alpha}^{\beta}\rangle + \eta_{\perp}|\Psi_{\alpha,\perp}^{\beta}\rangle. \quad (29)$$

Here, η_{\perp} denotes the norm of the orthogonal component, and $|\Psi_{\alpha,\perp}^{\beta}\rangle$ is a normalized vector orthogonal to $|\Psi_{\alpha}^{\beta}\rangle$. Unlike the parallel component, the orthogonal error does not cancel out through division. Therefore, the key to Trotter error resilience lies in the relative magnitudes of η_{\parallel} and η_{\perp} . Numerical tests in [Figure 8 \(c\)](#) demonstrate that $\eta_{\perp} \ll \eta_{\parallel}$ in practice. This dominance of the parallel component ensures that error cancellation through division remains effective, making the method robust against Trotter errors.

One notable point regarding noise resilience is that, in addition to the noise cancellation effect demonstrated in [Fig. 7-8](#), the use of the estimator in [Eq.\(8\)](#) enhances robustness against noise. This is because it computes only energy differences, limiting the influence of noise to the energy difference $E_{\alpha} - E_{\alpha-1}$. [Fig. 3 \(d\)](#) shows this. In this figure, we can see that the energy computed by [Eq. \(8\)](#) is more precise and stable compared to the energy computed by $\langle H_{\alpha} \rangle_{\alpha} = \langle \Phi_{\alpha} | H_{\alpha} | \Phi_{\alpha} \rangle$ using [Eq. \(5\)](#).

Another important note is that our discussion on noise resilience does not imply resilience to statistical noise. In fact, as the noise level increases, the impact of statistical error on the results is amplified, requiring a larger number of samples.

DISCUSSION

In this work, we introduced the quantum Zeno Monte Carlo (QZMC) for the emerging stepping stone era of quantum computing [12]. This method computes static and dynamical observables of gapped quantum systems within a polynomial quantum time, without the need for variational parameters. Leveraging the Quantum Zeno effect, we progressively approach the unknown eigenstate from the readily solvable Hamiltonian's eigenstate. This aspect distinguishes our method from other methods for phase estimations, which necessitate an initial state with significant overlap with the desired eigenstate [5, 6, 13, 14, 24, 25, 44]. Preparing a state with substantial overlap with an eigenstate of an easily solvable Hamiltonian is much simpler than preparing an initial state with non-trivial overlap with the unknown eigenstate, making our algorithm highly practical compared to other methods. Next characteristic of the algorithm is its computation of eigenstate properties by dividing the properties of the unnormalized eigenstate by its norm squared ([Eq. \(5\)](#)). We demonstrated that this approach effectively cancels out noise effects in the denominator and the numerator, rendering the method resilient to device noise as well as Trotter error. This resilience arises from the similar noise levels experienced by both the denominator and the numerator of observable expectation value, leading us to conclude that our approach is well-suited for homogeneous parallel quantum computing.

METHODS

NISQ simulation

Here, we provide the details of the NISQ simulations in Figs. 2-4. Throughout the simulations, we used $N_s = 4000$ shots for one- and two-qubit systems, and $N_s = 2048$ shots for the XXZ model. Since any 1- or 2-qubit unitary operation can be represented with a small number of gates [64], the consecutive time evolutions encountered in QZMC can be implemented within a shallow circuit with a few parameters. For the 1-qubit system, the parameters $\theta_1, \theta_2, \theta_3, \theta_4$ for the unitary matrix U are obtained from [64]:

$$U = e^{i\theta_4} \begin{bmatrix} \cos(\theta_1/2) & -\sin(\theta_1/2)e^{i\theta_3} \\ \sin(\theta_1/2)e^{i\theta_2} & \cos(\theta_1/2)e^{i(\theta_2+\theta_3)} \end{bmatrix}. \quad (30)$$

For the 2-qubit system, we applied the two-qubit Weyl decomposition [65], as implemented in Qiskit.

For the XXZ model, we set $\beta = \sqrt{2}$ and combined $(P_1^\beta)^2$ in Eq. (8) into a single integral. For Trotterization, we employed second-order Trotterization based on the efficient implementation of Trotterized quantum circuits [51], using two Trotter steps. We begin with XXZ dimers, described by the Hamiltonian

$$H_0 = -J \sum_{i;\text{odd}} (S_i^x S_{i+1}^x + S_i^y S_{i+1}^y + \Delta S_i^z S_{i+1}^z). \quad (31)$$

For systems with up to 8 qubits, we used the first-order perturbation energy as a predictor for the energy. For the 10-qubit system, we employed $E_2 + E_8$ as the predictor, where E_2 is the energy of a single XXZ dimer, and E_8 is the energy of an 8-site XXZ model computed using *ibm_torino*. Subsequently, using the computed E_{10} , we used $E_2 + E_{10}$ as the predictor for the 12-site XXZ model. We used an initialization circuit that prepares the vacuum state $|0^n\rangle$ when the ancilla qubit is in $|0\rangle$, and the ground state of H_0 when the ancilla qubit is in $|1\rangle$. The specific initialization circuit for the 10-site XXZ model is provided in the Supplementary Information. The number of gates used in this simulation, in terms of the basis gates of *ibm_torino*, is 237 for 4 sites, 384 for 6 sites, 534 for 8 sites, 696 for 10 sites, and 857 for 12 sites.

Noiseless simulation

Here, we discuss more detailed information about noiseless simulations (Figures 5-6). In these calculations, we consider the Hubbard model which is described by the Hamiltonian

$$H = - \sum_{\langle ij \rangle \sigma} t_{ij} c_{i\sigma}^\dagger c_{j\sigma} - \sum_i \mu (n_{i\uparrow} + n_{i\downarrow}) + \sum_i U n_{i\uparrow} n_{i\downarrow}, \quad (32)$$

with the chemical potential $\mu = U/2$, corresponding to the half-filling. The first two terms represent the kinetic energy and are denoted as H_t , while the last term represents electron-electron interaction and is referred to as H_U . The ground state

of the Hubbard dimer can be expressed as

$$|\Phi_{0,\text{dimer}}\rangle = \cos(\theta_d/2) |0011\rangle + \sin(\theta_d/2) |0110\rangle - \sin(\theta_d/2) |1001\rangle + \cos(\theta_d/2) |1100\rangle. \quad (33)$$

Here, the angle θ_d is given by

$$\theta_d = -2 \arctan \left(\frac{1}{2t} \left(\frac{U}{2} + \sqrt{\frac{U^2}{4} + 4t^2} \right) \right). \quad (34)$$

The ground state of H_0 , composed of a collection of dimers, is formed by the direct product of Eq. (33) for each dimer. The following describes the details specific to the calculations in Fig. 5, performed using the *cirq* quantum computer simulator. In the simulations, we used N_ν and Trotter steps (N_T) that varied with the system size, while fixing the number of shots at $N_s = 10,000$. Based on Eq. (22), N_ν was set proportional to $\|H'\|^2$, where

$$\|H'\| = t \times (\text{number of sites}) \quad (\text{for a chain}), \quad (35)$$

and

$$\|H'\| = \frac{4t}{\pi} \times (\text{number of sites}) \quad (\text{for a ladder}). \quad (36)$$

The proportionality constant was determined by testing the 6×1 system numerically. The first-order Trotterized time evolution $U_1(\tau)$ for the Hubbard model with n_T Trotter steps introduces a Trotter error [39] given by

$$\|e^{-iH\tau} - U_1(\tau)\| \leq \frac{\tau^2}{2n_T} \|[H_t, H_U]\|, \quad (37)$$

where

$$\|[H_t, H_U]\| \leq \sum_{\langle ij \rangle \sigma} t_{ij} U \|[c_{i\sigma}^\dagger c_{j\sigma}, \sum_i n_{i\uparrow} n_{i\downarrow}]\|. \quad (38)$$

Since all orbital indices are equivalent, $\|[c_{i\sigma}^\dagger c_{j\sigma}, \sum_i n_{i\uparrow} n_{i\downarrow}]\|$ remains constant for any i and j . Consequently,

$$\|[H_t, H_U]\| \leq CU(t_{\text{intra}} N_{\text{intra}} + t_{\text{inter}} N_{\text{inter}}), \quad (39)$$

where N_{intra} denotes the number of intra-dimer hoppings and N_{inter} represents the number of inter-dimer hoppings, and C is a proportionality constant.

Based on this, $N_{T,\alpha}$ was determined as

$$N_{T,\alpha} = \text{int} \left[75 \times \frac{(t_{\text{intra}} N_{\text{intra}} + t_{\text{inter},\alpha} N_{\text{inter}})}{8} \right], \quad (40)$$

with a minimum value of 20. Specific values of N_ν and total Trotter steps $N_T = 2 \sum_{\alpha=1}^{N_\alpha} N_{T,\alpha}$ for each model are summarized in Supplementary information.

Next, we provide detailed information on the comparative study for the Hubbard models in Fig. 6. In this case, we considered open boundary conditions, and the initial state is prepared from direct product of Eq. (33), with θ_d adjusted to achieve $|\langle \Phi | \Phi_0 \rangle|^2 = 0.4$.

For all data in Fig. 6, each calculation is repeated 30 times, and the absolute values of energy errors were averaged over repetitions. To measure the maximum time length T , we used the 99th percentile of the distribution of time evolution lengths, as all three methods are stochastic. This means that 99% of the time evolution lengths are smaller than T .

The computational parameters is set according to the references for the compared methods. For Lin and Tong's method [14], we set the parameter $\delta = 4/d$ as in the reference and varied d , which determines the time length. We used 1800 samples, consistent with the original paper. For QCELS [13], we followed the relative gap D estimation and parameter settings in the original article, using $d = \lfloor 15/D \rfloor$ and $N = 5$. The sample number for each $n\tau_j$ was set to 2048, higher than the values used in the original paper.

For QZMC, we used $N_\nu = 16,384$ for calculations with $\epsilon \geq 0.001$ and $N_\nu = 1,638,400$ for calculations with $\epsilon < 0.001$. For precise calculation, after obtaining the energy difference using Eq. (8), we recomputed it with the obtained E_α value at each α .

For the middle and bottom panels of Fig. 6, we noted that the maximum time evolution length T is set for each method to achieve a precision ϵ of about 0.003 under exact time evolution. In practice, the following parameters were used in our calculations.

For the 4-site Hubbard model with $U/t = 4$, we used $d = 4000$ for Lin and Tong's method, resulting in $T = 398.56$ and $\epsilon = 2.46 \times 10^{-3}$. For QCELS, we used $J = 5$ and $\tau_J = 40$, yielding $T = 23.09$ and $\epsilon = 2.45 \times 10^{-3}$. In QZMC, we used $\beta = 1.6$, which gave $T = 20.53$ and $\epsilon = 2.23 \times 10^{-3}$.

For the 4-site Hubbard model with $U/t = 10$, we used $d = 6000$ for Lin and Tong's method, leading to $T = 323.26$ and $\epsilon = 2.79 \times 10^{-3}$. In QCELS, we used $J = 7$ and $\tau_J = 108$, resulting in $T = 32.32$ and $\epsilon = 3.16 \times 10^{-3}$. For QZMC, we used $\beta = 2.6$, yielding $T = 33.36$ and $\epsilon = 3.24 \times 10^{-3}$.

For the 8-site Hubbard model with $U/t = 10$, we used $d = 12000$ for Lin and Tong's method, producing $T = 316.13$ and $\epsilon = 2.84 \times 10^{-3}$. In QCELS, we used $J = 9$ and $\tau_J = 372$, resulting in $T = 54.65$ and $\epsilon = 2.42 \times 10^{-3}$. For QZMC, we used $\beta = 4.2$, giving $T = 53.88$ and $\epsilon = 2.96 \times 10^{-3}$.

In the Trotterization tests, first-order Trotterization was employed for all methods. In QZMC, the Trotter steps $N_{T,\alpha}$ for each α were determined as

$$N_{T,\alpha} \propto (t_{\text{intra}}N_{\text{intra}} + t_{\text{inter}}N_{\text{inter}}), \quad (41)$$

and the total Trotter steps N_T were computed as $2 \sum_{\alpha} N_{T,\alpha}$. For calculations in Fig. 6, we used a shot number $N_s = 2048$.

DATA AVAILABILITY

The data generated and/or analyzed during this study are available from the corresponding author upon reasonable request.

CODE AVAILABILITY

The code developed during this study is available from the corresponding author upon reasonable request.

ACKNOWLEDGMENT

We thank Hyukjoon Kwon, Joonsuk Huh, and Lin Lin for their insightful comments and discussions. This research was supported by Quantum Simulator Development Project for Materials Innovation through the National Research Foundation of Korea (NRF) funded by the Korean government (Ministry of Science and ICT(MSIT))(No. NRF-2023M3K5A1094813). For one and two qubit simulations, we acknowledge the use of IBM Quantum services for this work and to advanced services provided by the IBM Quantum Researchers Program. The views expressed are those of the authors, and do not reflect the official policy or position of IBM or the IBM Quantum team. For larger system calculation, we used resources of the Center for Advanced Computation at Korea Institute for Advanced Study and the National Energy Research Scientific Computing Center (NERSC), a U.S. Department of Energy Office of Science User Facility operated under Contract No. DE-AC02-05CH11231. SC was supported by a KIAS Individual Grant (CG090601) at Korea Institute for Advanced Study. M.H. is supported by a KIAS Individual Grant (No. CG091301) at Korea Institute for Advanced Study.

AUTHOR CONTRIBUTIONS

M.H. conceived the original idea. M.H. and S.C. developed the idea into algorithms. M.H. implemented and performed classical as well as quantum computer calculation. M.H. established the analytical proof of the computational complexity. All authors contributed to the writing of the manuscript.

COMPETING INTERESTS

The authors declare no competing interests.

[1] P. Benioff, The computer as a physical system: A microscopic quantum mechanical hamiltonian model of computers as represented by Turing machines, *J. Stat. Phys.* **22**, 563 (1980).
 [2] R. P. Feynman, Simulating physics with computers, *Int. J. Theor. Phys.* **21** (1982).

[3] M. A. Nielsen and I. L. Chuang, *Quantum computation and quantum information* (Cambridge university press, 2010).
 [4] Y. Shen, D. Camps, A. Szasz, S. Darbha, K. Klymko, D. B. Williams-Young, N. M. Tubman, and R. V. Beeumen, Estimating eigenenergies from quantum dynamics: A unified noise-resilient measurement-driven approach, [arXiv:2306.01858](https://arxiv.org/abs/2306.01858)

- (2023).
- [5] A. Y. Kitaev, Quantum measurements and the abelian stabilizer problem, [arXiv:quant-ph/9511026](https://arxiv.org/abs/quant-ph/9511026) (1995).
 - [6] D. S. Abrams and S. Lloyd, Quantum algorithm providing exponential speed increase for finding eigenvalues and eigenvectors, *Phys. Rev. Lett.* **83**, 5162 (1999).
 - [7] P. W. Shor, Fault-tolerant quantum computation in *Proc. 37th Conference on Foundations of Computer Science* (IEEE, 1996), pp. 56-65.
 - [8] D. Gottesman, Theory of fault-tolerant quantum computation, *Phys. Rev. A* **57**, 127 (1998).
 - [9] J. Preskill, Quantum Computing in the NISQ era and beyond, *Quantum* **2**, 79 (2018).
 - [10] A. Peruzzo, J. McClean, P. Shadbolt, M.-H. Yung, X.-Q. Zhou, P. J. Love, A. Aspuru-Guzik, and J. L. O’Brien, A variational eigenvalue solver on a photonic quantum processor, *Nat. Commun* **5**, 4213 (2014).
 - [11] J. R. McClean, J. Romero, R. Babbush, and A. Aspuru-Guzik, The theory of variational hybrid quantum-classical algorithms, *New J. Phys.* **18**, 023023 (2016).
 - [12] D. Bluvstein, S. J. Evered, A. A. Geim, S. H. Li, H. Zhou, T. Manovitz, S. Ebadi, M. Cain, M. Kalinowski, D. Hangleiter, *et al.*, Logical quantum processor based on reconfigurable atom arrays, *Nature* **626**, 58 (2024).
 - [13] Z. Ding and L. Lin, Even shorter quantum circuit for phase estimation on early fault-tolerant quantum computers with applications to ground-state energy estimation, *PRX Quantum* **4**, 020331 (2023).
 - [14] L. Lin and Y. Tong, Heisenberg-limited ground-state energy estimation for early fault-tolerant quantum computers, *PRX Quantum* **3**, 010318 (2022).
 - [15] B. Misra and E. G. Sudarshan, The zeno’s paradox in quantum theory, *J. Math. Phys.* **18**, 756 (1977).
 - [16] R. D. Somma, S. Boixo, H. Barnum, and E. Knill, Quantum simulations of classical annealing processes, *Phys. Rev. Lett.* **101**, 130504 (2008).
 - [17] D. Poulin and P. Wocjan, Preparing ground states of quantum many-body systems on a quantum computer, *Phys. Rev. Lett.* **102**, 130503 (2009).
 - [18] S. Boixo, E. Knill, R. D. Somma, Eigenpath traversal by phase randomization., *Quantum Inf. Comput.* **9**, 833 (2009).
 - [19] H.-T. Chiang, G. Xu, and R. D. Somma, Improved bounds for eigenpath traversal, *Phys. Rev. A* **89**, 012314 (2014).
 - [20] L. Lin and Y. Tong, Optimal polynomial based quantum eigenstate filtering with application to solving quantum linear systems, *Quantum* **4**, 361 (2020).
 - [21] J. H. van Vleck, Nonorthogonality and ferromagnetism, *Phys. Rev.* **49**, 232 (1936).
 - [22] W. Kohn, Nobel lecture: Electronic structure of matter—wave functions and density functionals, *Rev. Mod. Phys.* **71**, 1253 (1999).
 - [23] P. Zeng, J. Sun, and X. Yuan, Universal quantum algorithmic cooling on a quantum computer, [arXiv:2109.15304](https://arxiv.org/abs/2109.15304) (2021).
 - [24] M. Huo and Y. Li, Error-resilient Monte Carlo quantum simulation of imaginary time, *Quantum* **7**, 916 (2023).
 - [25] G. Wang, D. S. França, R. Zhang, S. Zhu, and P. D. Johnson, Quantum algorithm for ground state energy estimation using circuit depth with exponentially improved dependence on precision, *Quantum* **7**, 1167 (2023).
 - [26] J. Sun, L. Vilchez-Estevéz, V. Vedral, A. T. Boothroyd, and M. Kim, Probing spectral features of quantum many-body systems with quantum simulators, [arXiv:2305.07649](https://arxiv.org/abs/2305.07649) (2023).
 - [27] S. Lloyd, Universal quantum simulators, *Science* **273**, 1073 (1996).
 - [28] C. Zalka, Simulating quantum systems on a quantum computer, *Proc. R. Soc. London, Ser. A* **454**, 313 (1998).
 - [29] D. P. Kroese, T. Taimre, and Z. I. Botev, *Handbook of Monte Carlo Methods* (John Wiley & Sons, 2011).
 - [30] M. T. Heath, *Scientific computing: an introductory survey, revised second edition* (SIAM, 2018).
 - [31] L. D. Landau and E. M. Lifshitz, *Quantum mechanics: non-relativistic theory*, Vol. 3 (Elsevier, 2013).
 - [32] V. Shende, S. Bullock, and I. Markov, Synthesis of quantum-logic circuits, *IEEE TCAD* **25**, 1000 (2006).
 - [33] J. Hubbard, Calculation of partition functions, *Phys. Rev. Lett.* **3**, 77 (1959).
 - [34] R. L. Stratonovich, On a Method of Calculating Quantum Distribution Functions, *Soviet Physics Doklady* **2**, 416 (1957).
 - [35] S. Zhang, Auxiliary-field quantum monte carlo for correlated electron systems, *Emergent Phenomena in Correlated Matter* (2013).
 - [36] S. Zhang and H. Krakauer, Quantum monte carlo method using phase-free random walks with slater determinants, *Phys. Rev. Lett.* **90**, 136401 (2003).
 - [37] M. Motta and S. Zhang, Ab initio computations of molecular systems by the auxiliary-field quantum monte carlo method, *Wiley Interdiscip. Rev. Comput. Mol. Sci.* **8**, e1364 (2018).
 - [38] D. Ceperley and B. Alder, Quantum monte carlo, *Science* **231**, 555 (1986),.
 - [39] A. M. Childs, Y. Su, M. C. Tran, N. Wiebe, and S. Zhu, Theory of trotter error with commutator scaling, *Phys. Rev. X* **11**, 011020 (2021).
 - [40] D. Layden, First-order trotter error from a second-order perspective, *Phys. Rev. Lett.* **128**, 210501 (2022).
 - [41] D. W. Berry, B. L. Higgins, S. D. Bartlett, M. W. Mitchell, G. J. Pryde, and H. M. Wiseman, How to perform the most accurate possible phase measurements, *Phys. Rev. A* **80**, 052114 (2009).
 - [42] B. L. Higgins, D. W. Berry, S. D. Bartlett, H. M. Wiseman, and G. J. Pryde, Entanglement-free heisenberg-limited phase estimation, *Nature* **450**, 393 (2007).
 - [43] R. D. Somma, Quantum eigenvalue estimation via time series analysis, *New J. Phys.* **21**, 123025 (2019).
 - [44] H. Ni, H. Li, and L. Ying, On low-depth algorithms for quantum phase estimation, *Quantum* **7**, 1165 (2023).
 - [45] R. F. Stewart, Small gaussian expansions of slater-type orbitals, *J. Chem. Phys.* **52**, 431 (1970).
 - [46] P. J. J. O’Malley, R. Babbush, I. D. Kivlichan, J. Romero, J. R. McClean, R. Barends *et al.*, Scalable quantum simulation of molecular energies, *Phys. Rev. X* **6**, 031007 (2016).
 - [47] M. Motta, C. Sun, A. T. Tan, M. J. O’Rourke, E. Ye, A. J. Minnich, F. G. Brandao, and G. K.-L. Chan, Determining eigenstates and thermal states on a quantum computer using quantum imaginary time evolution, *Nat. Phys.* **16**, 205 (2020).
 - [48] J. T. Seeley, M. J. Richard, and P. J. Love, The bravyi-kitaev transformation for quantum computation of electronic structure, *J. Chem. Phys.* **137** (2012).
 - [49] M. Steudtner and S. Wehner, Fermion-to-qubit mappings with varying resource requirements for quantum simulation, *New J. Phys.* **20**, 063010 (2018).
 - [50] J. Hubbard and B. H. Flowers, Electron correlations in narrow energy bands, *Proc. R. Soc. London, Ser. A* **276**, 238 (1963).
 - [51] T. A. Chowdhury, K. Yu, M. A. Shamim, M. L. Kabir, and R. S. Sufian, Enhancing quantum utility: Simulating large-scale quantum spin chains on superconducting quantum computers, *Phys. Rev. Res.* **6**, 033107 (2024).
 - [52] J. W. Negele and H. Orland, *Quantum many-particle systems*, Advanced book classics (Westview, Boulder, CO, 1988) addison-Wesley edition.

- [53] N. Ezzell, B. Pokharel, L. Tewala, G. Quiroz, and D. A. Lidar, Dynamical decoupling for superconducting qubits: A performance survey, *Phys. Rev. Appl.* **20**, 064027 (2023).
- [54] E. van den Berg, Z. K. Mineev, and K. Temme, Model-free readout-error mitigation for quantum expectation values, *Phys. Rev. A* **105**, 032620 (2022).
- [55] K. Temme, S. Bravyi, and J. M. Gambetta, Error mitigation for short-depth quantum circuits, *Phys. Rev. Lett.* **119**, 180509 (2017).
- [56] Y. Li and S. C. Benjamin, Efficient variational quantum simulator incorporating active error minimization, *Phys. Rev. X* **7**, 021050 (2017).
- [57] T. Giurgica-Tiron, Y. Hindy, R. LaRose, A. Mari, and W. J. Zeng, Digital zero noise extrapolation for quantum error mitigation, in *IEEE International Conference on Quantum Computing and Engineering* (IEEE, 2020) pp. 306–316.
- [58] S. Zhang, Y. Lu, K. Zhang, W. Chen, Y. Li, J.-N. Zhang, and K. Kim, Error-mitigated quantum gates exceeding physical fidelities in a trapped-ion system, *Nature communications* **11**, 587 (2020).
- [59] <https://quantumai.google/qsim>.
- [60] H. F. Trotter, On the product of semi-groups of operators, *Proc. Am. Math. Soc.* **10**, 545 (1959).
- [61] <https://www.ibm.com/quantum/qiskit>.
- [62] J. Tilly, H. Chen, S. Cao, D. Picozzi, K. Setia, Y. Li, E. Grant, L. Wossnig, I. Rungger, G. H. Booth, and J. Tennyson, The variational quantum eigensolver: A review of methods and best practices, *Phys. Rep.* **986**, 1 (2022),.
- [63] J. Watrous, Quantum computational complexity, [arXiv:0804.3401](https://arxiv.org/abs/0804.3401) (2008).
- [64] V. V. Shende, I. L. Markov, and S. S. Bullock, Minimal universal two-qubit controlled-not-based circuits, *Phys. Rev. A* **69**, 062321 (2004).
- [65] A. W. Cross, L. S. Bishop, S. Sheldon, P. D. Nation, and J. M. Gambetta, Validating quantum computers using randomized model circuits, *Phys. Rev. A* **100**, 032328 (2019).
- [66] W. J. Huggins, B. A. O’Gorman, N. C. Rubin, D. R. Reichman, R. Babbush, and J. Lee, Unbiasing fermionic quantum monte carlo with a quantum computer, *Nature* **603**, 416 (2022).

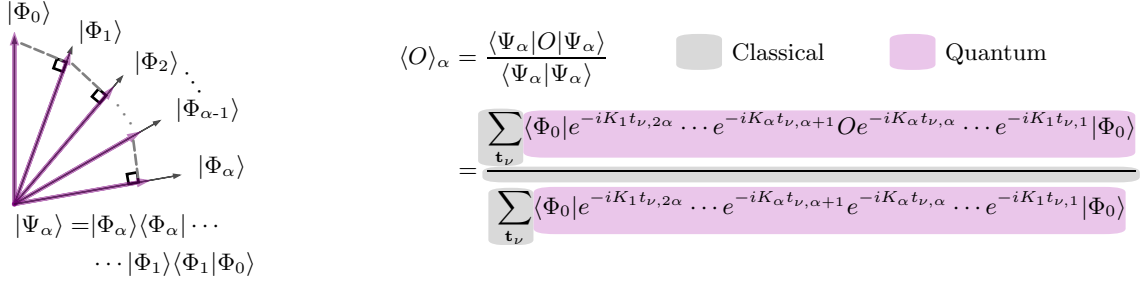


Figure 1. **Overview of the Quantum Zeno Monte Carlo.** The construction of the unnormalized eigenstate $|\Psi_\alpha\rangle$ of H_α from the eigenstate $|\Phi_0\rangle$ of H_0 is depicted (left). Each $|\Phi_k\rangle$ represents the normalized eigenstate of H_k . In the right, we present a summary of our Quantum Zeno Monte Carlo for computing the expectation value of an observable (O). First, classical computer generates a time vector $\mathbf{t}_\nu = [t_{\nu,1} \ t_{\nu,2} \ \dots \ t_{\nu,2\alpha}]^T$, where $t_{\nu,k}$ follows Gaussian distribution. Next, quantum computer measure the expectation value with the given time vector. Finally, the sum over N_ν Monte Carlo sampling as well as the division is conducted by using classical computer. Here, $K_{\alpha'}$ represents $H_{\alpha'} - E_{\alpha'}$.

Table I. Computational cost of QZMC and other quantum algorithms

	Maximum time evolution length	Total number of samples
QZMC	$\mathcal{O}(\Delta_g^{-2} (\log(\Delta_g^{-1} \epsilon^{-1} n))^{1/2} \text{poly}(n))$	$\mathcal{O}(\epsilon^{-2} \Delta_g^{-1} \text{poly}(n))$
QPE [41, 42]	$\tilde{\mathcal{O}}(\epsilon^{-1} p_0^{-1})$	$\tilde{\mathcal{O}}(p_0^{-1} \text{polylog}(\epsilon^{-1}))$
QEEA [43]	$\tilde{\mathcal{O}}(\epsilon^{-1} \text{polylog}(p_0^{-1}))$	$\tilde{\mathcal{O}}(\epsilon^{-3} p_0^{-2})$
Ref. [14]	$\tilde{\mathcal{O}}(\epsilon^{-1} \text{polylog}(p_0^{-1}))$	$\tilde{\mathcal{O}}(p_0^{-2} \text{polylog}(\epsilon^{-1}))$
Ref. [25]	$\mathcal{O}(\Delta_g^{-1} \text{polylog}(\epsilon^{-1} p_0^{-1} \Delta_g))$	$\mathcal{O}(p_0^{-2} \epsilon^{-2} \Delta_g^2)$

^a This table summarize the cost of QZMC to compute the ground state energy and compares it with several other quantum algorithms that computes the ground state energy within a single ancilla qubit. Complexity analysis of QPE and QEEA imported from Ref. [14]. Here, p_0 the probability of getting exact eigenstate from the initial states, ϵ is a desired precision in the energy, n is the number of qubits, and Δ_g is the lower bound of the energy gap between the ground and other states. Optimized algorithms for highly overlapped initial states [13, 44] shows similar dependence with algorithm of Ref. [14], only constant factor is different.

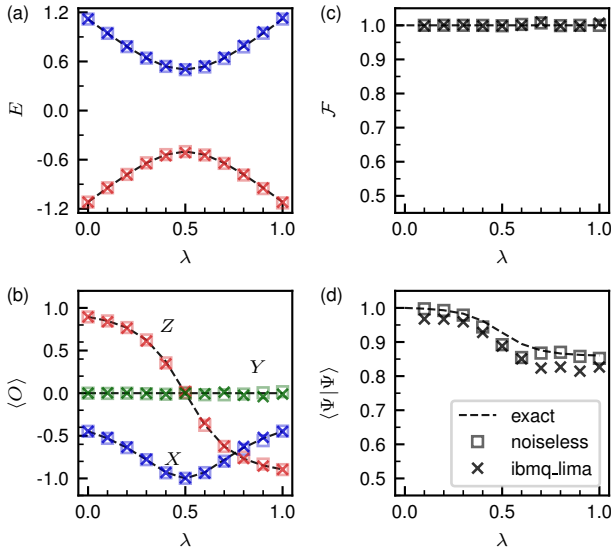


Figure 2. **A one-qubit system.** The energy eigenvalues of the ground (red) and the excited state (blue) are plotted in (a). In (b), we plotted $\langle X \rangle$ (blue), $\langle Y \rangle$ (green), and $\langle Z \rangle$ (red) calculated for the ground state. (c) and (d) display the fidelity \mathcal{F} and $\langle \Psi | \Psi \rangle$ for the ground state. In (a)-(d), dotted lines represent the exact result, boxes represent QZMC results with a noiseless simulator, and crosses represent results with *ibmq_lima*. In this figure, we used $\beta = 5$ and $N_\nu = 400$.

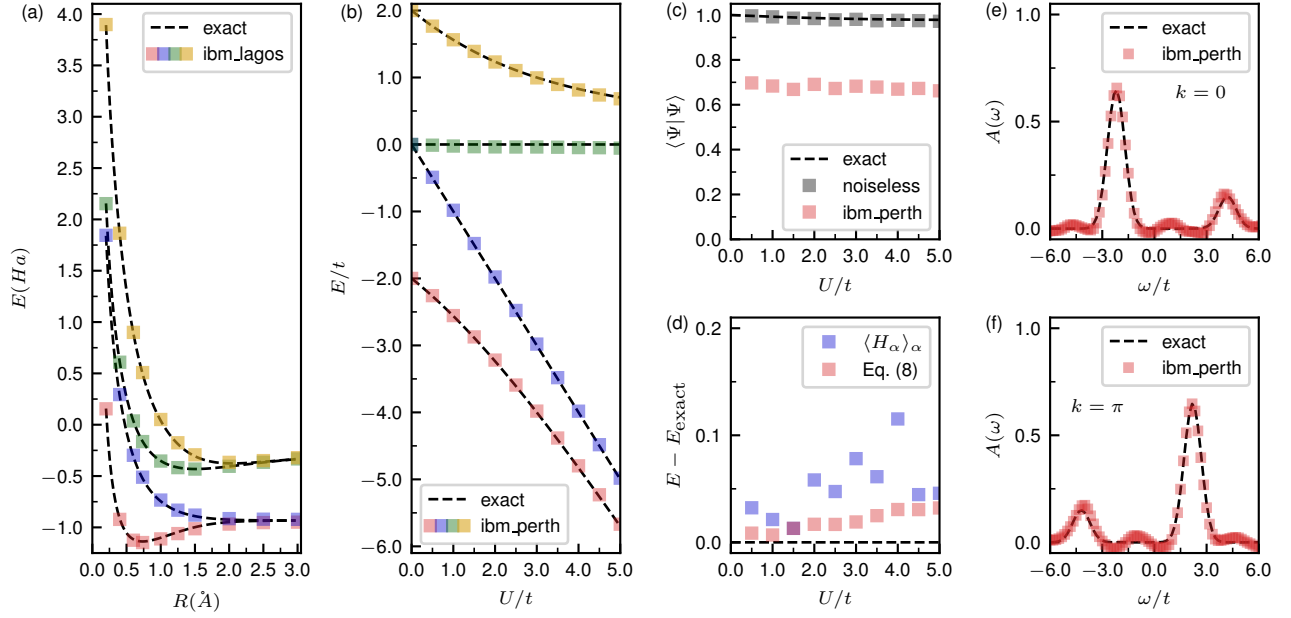


Figure 3. **\mathbf{H}_2 and the Hubbard dimer.** (a) plots energy eigenvalues of \mathbf{H}_2 in a STO-3G basis as a function of the bond length. Here, we used $\beta = 5$ and NISQ device calculation is conducted with *ibm_lagos*. In (b)-(f), we considered the Hubbard dimer. (b) shows energy eigenvalues as a function of the Coulomb interaction U . In (a) and (b), different states are distinguished by different colors. In (c), we compared $\langle \Psi | \Psi \rangle$ of the ground state calculated with the NISQ device with exact values and noiseless QZMC results. (d) compares two energy estimator $\langle H_\alpha \rangle_\alpha = \langle \Phi_\alpha | H_\alpha | \Phi_\alpha \rangle$ and Eq. (8). The spectral functions for two different crystal momentum (e) $k = 0$ and (f) $k = \pi$ are plotted. For the Hubbard dimer, we used $\beta = 0.5$ and *ibm_perth* is used. In this figure, we used $N_\nu = 100$ Monte Carlo samples for each α and the spectral function is calculated with 300 Monte Carlo samples.

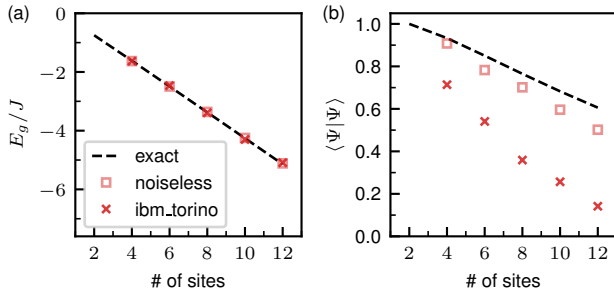


Figure 4. **NISQ simulation of XXZ model** (a) The energy eigenvalues and (b) $\langle \Psi | \Psi \rangle$ of XXZ model for various sizes from 4 to 12 qubits are plotted. In this figure, dotted lines represent the calculation with exact projection, boxes represent noiseless simulation result, and crosses are QZMC results with the *ibm_torino*. For QZMC, we used $\beta = \sqrt{2}$, $N_\alpha = 1$, and $N_\nu = 300$.

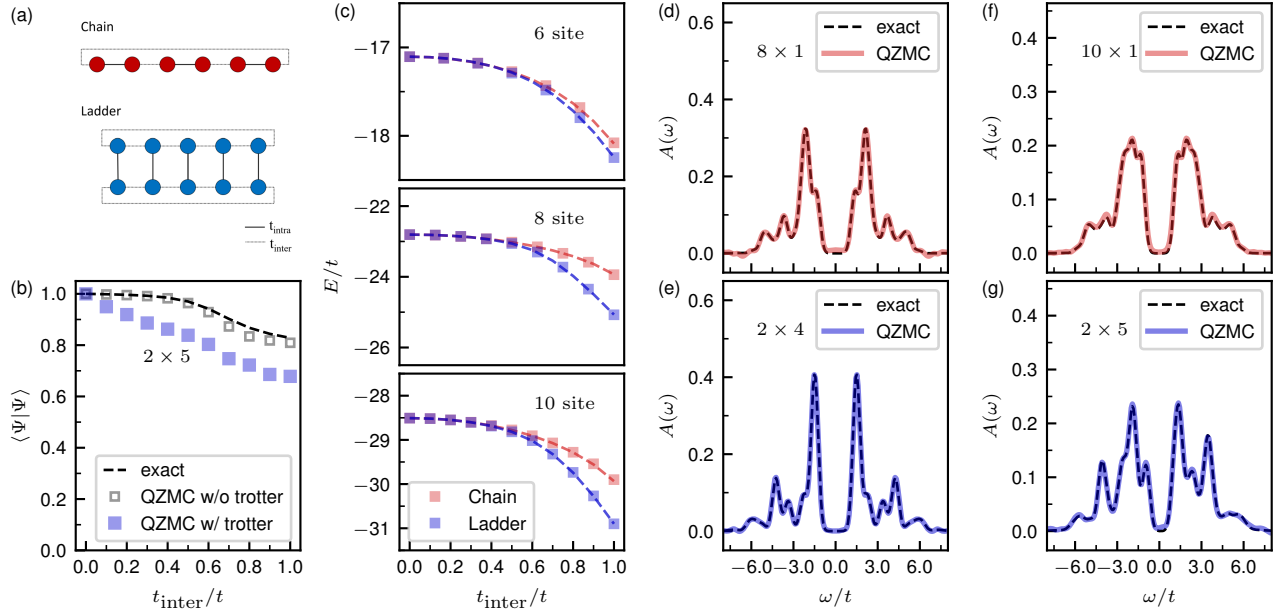


Figure 5. **The Hubbard model in various sizes.** (a) shows two geometries we considered. Here, colored circles denote sites, solid lines indicate intra-dimer hopping t_{intra} , and dotted lines represent inter-dimer hopping t_{inter} . (b) displays $\langle \Psi | \Psi \rangle$ for the 2×5 Hubbard model as a function of t_{inter} , while (c) presents ground state energy eigenvalues computed from QZMC. In each subplot of (c), red squares denote energies for 6×1 , 8×1 , and 10×1 models with QZMC, with red dotted lines indicating corresponding exact values. Blue squares and lines represent the same values for 2×3 , 2×4 , and 2×5 cases. (d)-(g) depict the local spectral function for the Hubbard models.

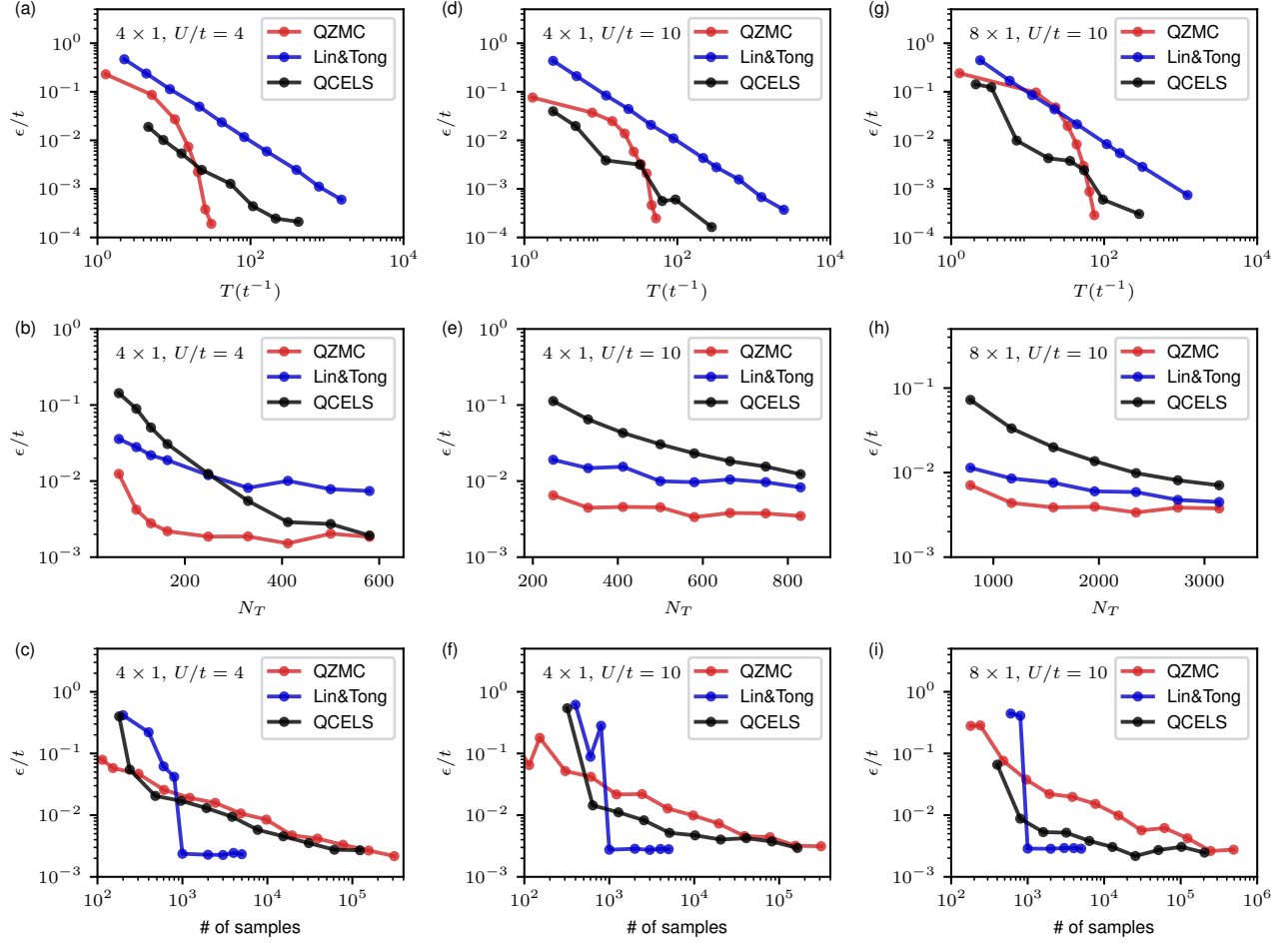


Figure 6. **Hubbard chains with various methods.** Ground energy estimation errors are shown for: (a)-(c) $U/t = 4$, 4 sites; (d)-(f) $U/t = 10$, 4 sites; and (g)-(i) $U/t = 10$, 8 sites. The figures plot the energy estimation error ϵ as a function of (a, d, g) the maximum time evolution length, (b, e, h) the total number of Trotter steps, and (c, f, i) the total number of samples. In all panels, blue points represent results from the method of Lin and Tong [14], black points represent results from QCELS [13], and red points represent results from QZMC.

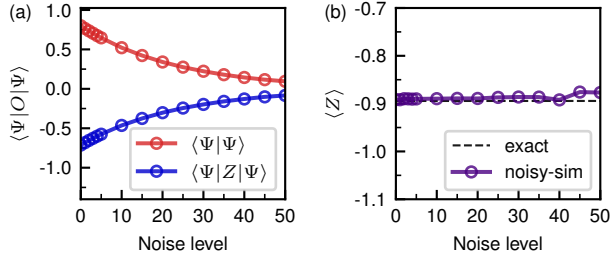


Figure 7. **Device noise resilience of QZMC.** $\langle \Psi | \Psi \rangle$, $\langle \Psi | Z | \Psi \rangle$, and $\langle Z \rangle$ of the one-qubit system considered in the Fig. 2 are drawn as a function of the noise level. The calculations are conducted with the qiskit noisy simulator using the noise model of *ibmq lima*. In this figure, we used $N_\alpha = 10$, $\beta = 5$ and $N_\nu = 400$.

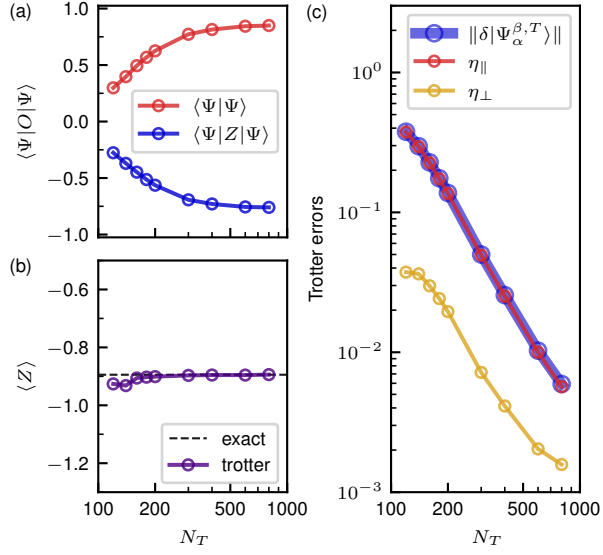


Figure 8. **Trotter Error resilience of QZMC.** (a)-(b) show $\langle \Psi | \Psi \rangle$, $\langle \Psi | Z | \Psi \rangle$, and $\langle Z \rangle$ as functions of the total number of Trotter steps, for the one-qubit system considered in Fig. 2. In (a)-(b), $N_\nu = 400$ was used. (c) displays the total Trotter error $\|\delta | \Psi_\alpha^{\beta, T} \rangle\|$, the parallel component η_{\parallel} , and the orthogonal component η_{\perp} , plotted against the total number of Trotter steps. For (c), $N_\nu = 4000$ was used to reduce the statistical error. In all panels, we set $N_\alpha = 10$ and $\beta = 5$.

Supplementary information for “Quantum Zeno Monte Carlo for computing observables”

Mancheon Han,^{1,*} Hyowon Park,^{2,3,†} and Sangkook Choi^{1,‡}

¹*School of Computational Sciences, Korea Institute for Advanced Study (KIAS), Seoul, 02455, Korea*

²*Materials Science Division, Argonne National Laboratory, Argonne, IL, 60439, USA*

³*Department of Physics, University of Illinois at Chicago, Chicago, IL, 60607, USA*

(Dated: January 7, 2025)

I. EQUATIONS FOR QUANTUM ZENO MONTE CARLO

This section provides more details of [Quantum Zeno Monte Carlo](#).

A. Monte Carlo Calculation of the Energy Difference

Following the same steps used to derive Eq. (7), we obtain the Monte Carlo formula for the numerator in Eq. (8):

$$\begin{aligned} & \langle \Psi_\alpha^\beta | \Phi_\alpha \rangle \langle \Phi_\alpha | (H_\alpha - H_{\alpha-1}) | \Psi_{\alpha-1}^\beta \rangle = \\ & \frac{1}{N_\nu} \sum_{\mathbf{t}_\nu} \langle \Phi_0 | e^{-iK_1 t_{\nu,2\alpha}} e^{-iK_2 t_{\nu,2\alpha-1}} \dots e^{-iK_\alpha t_{\nu,\alpha+1}} \\ & e^{-iK_\alpha t_{\nu,\alpha}} (H_\alpha - H_{\alpha-1}) e^{-iK_{\alpha-1} t_{\nu,\alpha-1}} \\ & e^{-iK_{\alpha-2} t_{\nu,\alpha-2}} \dots e^{-iK_1 t_{\nu,1}} | \Phi_0 \rangle. \end{aligned} \quad (\text{S.1})$$

The measurement of the integrands on a quantum computer can be achieved using the Pauli string expansion of the operator $(H_\alpha - H_{\alpha-1})$ [62].

B. Green’s function

We derive the Quantum Zeno Monte Carlo (QZMC) method for computing the electronic Green’s function. The computation of other Green’s functions, such as the spin-spin correlation function, follows a similar approach.

The retarded electronic Green’s function is defined as

$$G_{jk}^R(t) = -i\theta(t) \langle \Phi | \{c_j(t), c_k^\dagger(0)\} | \Phi \rangle, \quad (\text{S.2})$$

where $\{, \}$ represents the anticommutator, and c_j (c_j^\dagger) is the annihilation (creation) operator for the j -th orbital. This function can be expressed in terms of the spectral function $A_{jk}(\omega)$ as

$$G_{jk}^R(\omega + i0^+) = \int_{-\infty}^{\infty} \frac{A_{jk}(\omega')}{\omega + i0^+ - \omega'} d\omega'. \quad (\text{S.3})$$

The spectral function $A_{jk}(\omega)$ is expanded as [52]

$$A_{jk}(\omega) = A_{jk,1}(\omega) + A_{jk,2}(\omega), \quad (\text{S.4})$$

where

$$\begin{aligned} A_{jk,1}(\omega) &= \sum_m \langle \Phi | c_j | m \rangle \langle m | c_k^\dagger | \Phi \rangle \delta(\mathcal{E}_m - \mathcal{E}_\Phi - \omega), \\ A_{jk,2}(\omega) &= \sum_m \langle \Phi | c_k^\dagger | m \rangle \langle m | c_j | \Phi \rangle \delta(\mathcal{E}_m - \mathcal{E}_\Phi + \omega). \end{aligned} \quad (\text{S.5})$$

Here, $|m\rangle$ and \mathcal{E}_m denote the energy eigenstates and their corresponding eigenvalues. We focus on computing $A_{jk,1}(\omega)$, as $A_{jk,2}(\omega)$ can be computed similarly. The Dirac delta function $\delta(x)$ is approximated using a Gaussian function:

$$\delta(x) \approx \frac{1}{\sqrt{2\pi\sigma^2}} e^{-x^2/2\sigma^2}. \quad (\text{S.6})$$

With Gaussian broadening, $A_{jk,1}(\omega)$ is computed as

$$A_{jk,1}(\omega) = \frac{1}{\sqrt{2\pi\sigma^2}} \langle \Phi | c_j e^{-(H - \mathcal{E}_\Phi - \omega)^2/2\sigma^2} c_k^\dagger | \Phi \rangle. \quad (\text{S.7})$$

We consider the Green’s function at α . Similar to Eq. (5), $A_{jk,1}(\omega)$ can be expressed as

$$A_{jk,1}(\omega) = \frac{1}{\sqrt{2\pi\sigma^2}} \frac{\tilde{A}_{jk,1}(\omega)}{\langle \Psi_\alpha | \Psi_\alpha \rangle}, \quad (\text{S.8})$$

where

$$\tilde{A}_{jk,1}(\omega) = \langle \Psi_\alpha | c_j e^{-(H_\alpha - E_\alpha - \omega)^2/2\sigma^2} c_k^\dagger | \Psi_\alpha \rangle. \quad (\text{S.9})$$

Using a Fourier expansion of $e^{-(H_\alpha - E_\alpha - \omega)^2/2\sigma^2}$, $\tilde{A}_{jk,1}(\omega)$ can be computed via Monte Carlo sampling, similar to Eq. (7):

$$\tilde{A}_{jk,1}(\omega) = \frac{1}{N_\nu} \sum_{\mathbf{t}_\nu} g_\alpha(c_j, c_k^\dagger, \mathbf{t}_\nu) e^{i\phi_\alpha(\mathbf{t}_\nu, \omega)}, \quad (\text{S.10})$$

where

$$\begin{aligned} g_\alpha(O_1, O_2, \mathbf{t}) &= \langle \Phi_0 | e^{-iH_1 t_{2\alpha+1}} e^{-iH_2 t_{2\alpha}} \dots \\ & e^{-iH_\alpha t_{\alpha+2}} O_1 e^{-iH_\alpha t_{\alpha+1}} O_2 e^{-iH_\alpha t_\alpha} \\ & e^{-iH_{\alpha-1} t_{\alpha-1}} \dots e^{-iH_1 t_1} | \Phi_0 \rangle, \end{aligned} \quad (\text{S.11})$$

and $\phi_\alpha(\mathbf{t}, \omega) = \sum_{\alpha'=1}^{\alpha} E_{\alpha'} (t_{\alpha'} + t_{2\alpha+2-\alpha'}) + (E_\alpha + \omega) t_{\alpha+1}$. Here, $t_{\nu, \alpha+1} \sim \mathcal{N}(0, 1/\sigma)$, and $t_{\nu, \alpha'} \sim \mathcal{N}(0, \beta)$ for all $\alpha' \neq \alpha + 1$. Since $g_\alpha(O_1, O_2, \mathbf{t})$ is independent of ω , $A_{jk}(\omega)$ can be computed for any ω by storing $g_\alpha(c_j, c_k^\dagger, \mathbf{t}_\nu)$.

* mchan@kias.re.kr

† hyowon@uic.edu

‡ sangkookchoi@kias.re.kr

II. SUPPLEMENT TO THE ERROR ANALYSIS AND COST ESTIMATION

This section provides additional details on Error analysis and Cost estimation in the main text. As noted in the main text, we consider the Hamiltonian $H(\lambda) = H_0 + \lambda H'$, starting with $|\Phi_0\rangle$, an eigenstate of $H_0 = H(\lambda = 0)$ with eigenvalue E_0 . For simplicity, we assume that $|\Phi(\lambda)\rangle$, which is adiabatically connected to $|\Phi_0\rangle$, is non-degenerate and has an eigenvalue $E(\lambda)$ satisfying $|E(\lambda) - \mathcal{E}_m(\lambda)| \geq \Delta_g$ for all other eigenenergies $\mathcal{E}_m(\lambda)$ of $H(\lambda)$. We then define $H_\alpha = H(\lambda_\alpha)$ for $\alpha = 1, 2, \dots, N_\alpha$, with $\lambda_\alpha = \alpha/N_\alpha$, as described in the main text. For simplicity, we denote $E_\alpha = E(\lambda_\alpha)$ and $|\Phi_\alpha\rangle = |\Phi(\lambda_\alpha)\rangle$. The eigenvectors of H_α are denoted by $|m_\alpha\rangle$, with corresponding eigenvalues $\mathcal{E}_{m,\alpha}$. In particular, $\mathcal{E}_{m_\alpha} = E_\alpha$ when $m_\alpha = \Phi_\alpha$.

A. Error analysis of $\langle \Psi_\alpha^\beta | \Psi_\alpha^\beta \rangle$

1. The number of projections

First, we derive Eq. (10) in the main text,

$$|\langle \Phi_\alpha | \Phi_{\alpha+1} \rangle|^2 \geq 1 - \|H'\|^2 \Delta_g^{-2} N_\alpha^{-2}, \quad (\text{S.12})$$

using the perturbation theory [31]. Starting from $H_{\alpha+1} = H_\alpha + \Delta\lambda H'$, we expand $|\Phi_{\alpha+1}\rangle$ as

$$|\Phi_{\alpha+1}\rangle = |\Phi_\alpha\rangle + (\Delta\lambda) |\Phi_\alpha^{(1)}\rangle + \frac{(\Delta\lambda)^2}{2} |\Phi_\alpha^{(2)}\rangle, \quad (\text{S.13})$$

omitting higher-order terms. Similarly, with $E_{\alpha+1} = E_\alpha + \Delta\lambda E'_\alpha + (\Delta\lambda)^2/2E''_\alpha + \dots$, and collecting $\Delta\lambda$ -order terms from $H_{\alpha+1} |\Phi_{\alpha+1}\rangle = E_{\alpha+1} |\Phi_{\alpha+1}\rangle$, we obtain

$$(E_\alpha - H_\alpha) |\Phi_\alpha^{(1)}\rangle = (H' - E'_\alpha) |\Phi_\alpha\rangle. \quad (\text{S.14})$$

Taking the inner product with $|m_\alpha\rangle$ on both sides gives

$$\langle m_\alpha | \Phi_\alpha^{(1)} \rangle = \frac{\langle m_\alpha | H' | \Phi_\alpha \rangle}{E_\alpha - \mathcal{E}_{m,\alpha}}, \quad \text{for } m_\alpha \neq \Phi_\alpha. \quad (\text{S.15})$$

Since $|\Phi_{\alpha+1}\rangle$ is normalized, $\langle \Phi_{\alpha+1} | \Phi_{\alpha+1} \rangle$ must not include $\Delta\lambda$ -dependent terms. And to uniquely define the phase of $|\Phi_{\alpha+1}\rangle$, we set $\langle \Phi_{\alpha+1} | \Phi_\alpha \rangle$ to be real. Then,

$$\begin{aligned} \langle \Phi_\alpha^{(1)} | \Phi_\alpha \rangle + \langle \Phi_\alpha | \Phi_\alpha^{(1)} \rangle &= 2 \langle \Phi_\alpha | \Phi_\alpha^{(1)} \rangle = 0, \\ \langle \Phi_\alpha | \Phi_\alpha^{(2)} \rangle + \langle \Phi_\alpha^{(1)} | \Phi_\alpha^{(1)} \rangle &= 0. \end{aligned} \quad (\text{S.16})$$

This yields

$$\langle \Phi_\alpha | \Phi_\alpha^{(2)} \rangle = - \sum_{m_\alpha \neq \Phi_\alpha} \frac{|\langle m_\alpha | H' | \Phi_\alpha \rangle|^2}{(E_\alpha - \mathcal{E}_{m,\alpha})^2}. \quad (\text{S.17})$$

Using this result, we have

$$\begin{aligned} \langle \Phi_\alpha | \Phi_{\alpha+1} \rangle &= 1 - \frac{(\Delta\lambda)^2}{2} \sum_{m_\alpha \neq \Phi_\alpha} \frac{|\langle m_\alpha | H' | \Phi_\alpha \rangle|^2}{(E_\alpha - \mathcal{E}_{m,\alpha})^2}, \\ \langle m_\alpha | \Phi_{\alpha+1} \rangle &= \Delta\lambda \frac{\langle m_\alpha | H' | \Phi_\alpha \rangle}{E_\alpha - \mathcal{E}_{m,\alpha}}, \quad \text{for } m_\alpha \neq \Phi_\alpha, \end{aligned} \quad (\text{S.18})$$

to leading order in $\Delta\lambda = \lambda_{\alpha+1} - \lambda_\alpha$. Since $|\mathcal{E}_{m,\alpha} - E_\alpha| \geq \Delta_g$,

$$\sum_{m_\alpha \neq \Phi_\alpha} \frac{|\langle m_\alpha | H' | \Phi_\alpha \rangle|^2}{(E_\alpha - \mathcal{E}_{m,\alpha})^2} \leq \frac{1}{\Delta_g^2} \|H'\|^2. \quad (\text{S.19})$$

Here, we use the matrix norm induced by the vector 2-norm [30], defined as $\|A\| = \sup_{\|x\|=1} \|Ax\|$. Combining Eq. (S.18) and Eq. (S.19), we obtain Eq. (S.12).

Next, we consider the ground state. Returning to perturbative analysis and collecting $(\Delta\lambda)^2$ -order terms in $\langle \Phi_\alpha | H_{\alpha+1} | \Phi_{\alpha+1} \rangle = E_{\alpha+1} \langle \Phi_\alpha | \Phi_{\alpha+1} \rangle$, we find

$$\frac{1}{2} E''_\alpha = \langle \Phi_\alpha | H' | \Phi_\alpha^{(1)} \rangle = \sum_{m_\alpha \neq \Phi_\alpha} \frac{|\langle m_\alpha | H' | \Phi_\alpha \rangle|^2}{(E_\alpha - \mathcal{E}_{m,\alpha})}. \quad (\text{S.20})$$

For a ground state, $|E_\alpha - \mathcal{E}_{m,\alpha}| \geq \Delta_g$ gives $E_\alpha - \mathcal{E}_{m,\alpha} \leq -\Delta_g$, $(E_\alpha - \mathcal{E}_{m,\alpha})^2 \geq -\Delta_g(E_\alpha - \mathcal{E}_{m,\alpha})$. Thus,

$$\begin{aligned} \langle \Phi_\alpha | \Phi_{\alpha+1} \rangle &= 1 - \frac{(\Delta\lambda)^2}{2} \sum_{m_\alpha \neq \Phi_\alpha} \frac{|\langle m_\alpha | H' | \Phi_\alpha \rangle|^2}{(E_\alpha - \mathcal{E}_{m,\alpha})^2} \\ &\geq 1 + \frac{(\Delta\lambda)^2}{4} \frac{E''(\lambda_\alpha)}{\Delta_g}. \end{aligned} \quad (\text{S.21})$$

This implies

$$\begin{aligned} \langle \Psi_\alpha | \Psi_\alpha \rangle &\geq 1 + \frac{1}{\Delta_g} \sum_{\alpha} \frac{E''(\lambda_\alpha)}{2N_\alpha^2} \\ &= 1 + \frac{1}{\Delta_g} \frac{(E'(1) - E'(0))}{2N_\alpha} + \mathcal{O}\left(\frac{1}{N_\alpha^2}\right). \end{aligned} \quad (\text{S.22})$$

Since $|E'(\lambda)| = |\langle \Phi(\lambda) | H' | \Phi(\lambda) \rangle| \leq \|H'\|$, we conclude

$$\langle \Psi_\alpha | \Psi_\alpha \rangle \geq 1 - \frac{\|H'\|}{\Delta_g} \frac{1}{N_\alpha}, \quad (\text{S.23})$$

to leading order in $1/N_\alpha$. Therefore, for the ground state, it is sufficient to have

$$N_\alpha \geq \frac{\|H'\|}{\Delta_g} \frac{1}{\eta_0}, \quad (\text{S.24})$$

to ensure $\| |\Psi_\alpha\rangle \|^2 \geq 1 - \eta_0$.

2. The projection errors

As defined in the main text, the error in the projected state is

$$|\delta\Psi_\alpha^\beta\rangle = |\Psi_\alpha^\beta\rangle - |\Psi_\alpha\rangle = (\mathcal{P}_\alpha^\beta - \mathcal{P}_\alpha) |\Phi_0\rangle. \quad (\text{S.25})$$

Here, we show Eq. (12) in the main text,

$$\| |\delta\Psi_\alpha^\beta\rangle \| \leq \frac{\alpha}{N_\alpha} e^{-\beta^2 \Delta_g^2 / 2} \frac{\|H'\|}{\Delta_g}, \quad (\text{S.26})$$

using an inductive argument. For convenience, we define $\delta\mathcal{P}_\alpha^\beta = \mathcal{P}_\alpha^\beta - \mathcal{P}_\alpha$, $P_\alpha^\beta = P_{H_\alpha}^\beta(E_\alpha)$, and $\delta P_\alpha^\beta = P_\alpha^\beta - |\Phi_\alpha\rangle\langle\Phi_\alpha|$. Then, up to the leading order in $1/N_\alpha$, we have

$$\begin{aligned} \|\delta P_\alpha^\beta |\Psi_{\alpha-1}\rangle\|^2 &= \langle\Psi_{\alpha-1}|(\delta P_\alpha^\beta)^2|\Psi_{\alpha-1}\rangle \\ &\leq (\Delta\lambda)^2 \sum_{m_\alpha \neq \Phi_\alpha} e^{-\beta^2(\mathcal{E}_{m,\alpha} - E_\alpha)^2} \frac{|\langle\Phi_\alpha|H'|m_\alpha\rangle|^2}{(\mathcal{E}_{m,\alpha} - E_\alpha)^2}, \end{aligned} \quad (\text{S.27})$$

by applying perturbation from H_α to $H_{\alpha-1}$, which results in Eq. (S.18) but with a reversed sign for $\Delta\lambda$. Because $\exp(-\beta^2 x^2)/x^2$ is a decreasing function, we obtain

$$\|\delta P_\alpha^\beta |\Psi_{\alpha-1}\rangle\| \leq \frac{1}{N_\alpha} e^{-\beta^2 \Delta_g^2/2} \frac{\|H'\|}{\Delta_g}. \quad (\text{S.28})$$

For $\alpha = 1$, this directly gives Eq. (S.26). Now, suppose that for some α ,

$$\|\delta\Psi_\alpha^\beta\| \leq \frac{\alpha}{N_\alpha} e^{-\beta^2 \Delta_g^2/2} \frac{\|H'\|}{\Delta_g}.$$

Then, using

$$|\delta\Psi_{\alpha+1}^\beta\rangle = \delta P_{\alpha+1}^\beta |\Psi_\alpha\rangle + P_{\alpha+1}^\beta |\delta\Psi_\alpha^\beta\rangle, \quad (\text{S.29})$$

and the inequality $\|v_1 + v_2\| \leq \|v_1\| + \|v_2\|$, we have

$$\begin{aligned} \|\delta\Psi_{\alpha+1}^\beta\rangle\| &\leq \|\delta P_{\alpha+1}^\beta |\Psi_\alpha\rangle\| + \|P_{\alpha+1}^\beta |\delta\Psi_\alpha^\beta\rangle\| \\ &\leq \frac{\alpha+1}{N_\alpha} e^{-\beta^2 \Delta_g^2/2} \frac{\|H'\|}{\Delta_g}, \end{aligned} \quad (\text{S.30})$$

where the second inequality follows from Eq. (S.28). This proves Eq. (S.26).

3. The trotterization errors

Let us define $|\psi_\alpha(\mathbf{t})\rangle = \exp(-iH_\alpha t_\alpha) \exp(-iH_{\alpha-1} t_{\alpha-1}) \cdots \exp(-iH_1 t_1) |\Phi_0\rangle$ and $|\psi_\alpha^T(\mathbf{t})\rangle$ as its trotterized version, such that $|\psi_\alpha^T(\mathbf{t})\rangle = \tilde{U}_\alpha(t_\alpha) \tilde{U}_{\alpha-1}(t_{\alpha-1}) \cdots \tilde{U}_1(t_1) |\Phi_0\rangle$, where $\tilde{U}_\alpha(t_\alpha)$ is the Trotterized approximation of $\exp(-iH_\alpha t_\alpha)$. The difference $|\delta\Psi_\alpha^{\beta,T}\rangle = |\Psi_\alpha^{\beta,T}\rangle - |\Psi_\alpha^\beta\rangle$ can be expressed as

$$\begin{aligned} |\delta\Psi_\alpha^{\beta,T}\rangle &= \frac{1}{(2\pi\beta^2)^{\alpha/2}} \int e^{-\sum_{\alpha'=1}^\alpha t_{\alpha'}^2/(2\beta^2) + i\phi_\alpha(\mathbf{t})} \\ &\quad \times (|\psi_\alpha^T(\mathbf{t})\rangle - |\psi_\alpha(\mathbf{t})\rangle) dt, \end{aligned} \quad (\text{S.31})$$

while $\phi_\alpha = \sum_{\alpha'=1}^\alpha E_{\alpha'} t_{\alpha'}$. Letting $\delta\tilde{U}_\alpha(t_\alpha) = \tilde{U}_\alpha(t_\alpha) - \exp(-iH_\alpha t_\alpha)$, we have [39]:

$$\|\delta\tilde{U}_\alpha(t_\alpha)\| \leq C_{\alpha,p} \frac{|t_\alpha|^{1+p}}{N_{T,\alpha}^p}, \quad (\text{S.32})$$

where p is the Trotterization order, $N_{T,\alpha}$ is the number of Trotter steps for the α -th evolution, and $C_{\alpha,p}$ is the coefficient

that is proportional to the sum of the norms of the commutators [39]. Thus,

$$\|\delta\tilde{U}_\alpha(t_\alpha) |\psi_{\alpha-1}(\mathbf{t})\rangle\| \leq C_{\alpha,p} \frac{|t_\alpha|^{1+p}}{N_{T,\alpha}^p}. \quad (\text{S.33})$$

Using an inductive argument similar to that in the proof of Eq. (S.26), we find

$$\| |\psi_\alpha^T(\mathbf{t})\rangle - |\psi_\alpha(\mathbf{t})\rangle \| \leq \sum_{\alpha'=1}^\alpha C_{\alpha',p} \frac{|t_{\alpha'}|^{1+p}}{N_{T,\alpha'}^p}. \quad (\text{S.34})$$

Substituting this into Eq. (S.31), we have

$$\begin{aligned} \|\delta\Psi_\alpha^{\beta,T}\rangle\| &\leq \sum_{\alpha'=1}^\alpha C_{\alpha',p} \frac{M_{1+p}(\beta)}{N_{T,\alpha'}^p}, \\ M_{1+p}(\beta) &= \frac{1}{\sqrt{2\pi\beta^2}} \int_{-\infty}^{\infty} e^{-t^2/(2\beta^2)} |t|^{1+p} dt. \end{aligned} \quad (\text{S.35})$$

By choosing $N_{T,\alpha}$ to be proportional to $C_{\alpha,p}^{1/p} M_{1+p}^{1/p}(\beta)$, we have

$$N_{T,\alpha} = \frac{C_{\alpha,p}^{1/p} M_{1+p}^{1/p}(\beta)}{\sum_{\alpha'=1}^{N_\alpha} C_{\alpha',p}^{1/p} M_{1+p}^{1/p}(\beta)} \frac{N_T}{2}, \quad (\text{S.36})$$

while total number of trotter steps $N_T = \sum_{\alpha=1}^{N_\alpha} N_{T,\alpha}$. Then,

$$\|\delta\Psi_\alpha^{\beta,T}\rangle\| \leq \alpha \frac{\left(\sum_{\alpha'=1}^{N_\alpha} C_{\alpha',p}^{1/p} M_{1+p}^{1/p}(\beta)\right)^p}{(N_T/2)^p}. \quad (\text{S.37})$$

By setting this bound smaller than $\eta_T/2$ at $\alpha = N_\alpha$, we obtain Eq. (15).

B. Error analysis of E_α

1. The projection errors

The numerator in Eq. (8) has an error of $\Delta\epsilon_\beta \langle\Psi_\alpha^\beta|\Psi_\alpha^\beta\rangle$, given by

$$\begin{aligned} \Delta\epsilon_\beta \langle\Psi_\alpha^\beta|\Psi_\alpha^\beta\rangle &= \langle\Psi_{\alpha-1}^\beta|(P_\alpha^\beta)^2 \Delta\lambda H' |\Psi_{\alpha-1}^\beta\rangle \\ &\quad - \langle\Psi_{\alpha-1}^\beta|(P_\alpha^\beta)^2 (E_\alpha - E_{\alpha-1}) |\Psi_{\alpha-1}^\beta\rangle. \end{aligned} \quad (\text{S.38})$$

Substituting $|\Psi_{\alpha-1}^\beta\rangle = |\Psi_{\alpha-1}\rangle + |\delta\Psi_{\alpha-1}^\beta\rangle$, we can expand Eq. (S.38) as

$$\begin{aligned} \Delta\epsilon_\beta \langle\Psi_\alpha^\beta|\Psi_\alpha^\beta\rangle &= \langle\delta\Psi_{\alpha-1}^\beta|(P_\alpha^\beta)^2 \Delta\lambda H' |\Psi_{\alpha-1}\rangle \\ &\quad + \langle\Psi_{\alpha-1}|(P_\alpha^\beta)^2 \Delta\lambda H' |\delta\Psi_{\alpha-1}^\beta\rangle \\ &\quad - \langle\delta\Psi_{\alpha-1}^\beta|(P_\alpha^\beta)^2 (E_\alpha - E_{\alpha-1}) |\Psi_{\alpha-1}\rangle \\ &\quad - \langle\Psi_{\alpha-1}|(P_\alpha^\beta)^2 (E_\alpha - E_{\alpha-1}) |\delta\Psi_{\alpha-1}^\beta\rangle, \end{aligned} \quad (\text{S.39})$$

up to the leading order of $\|\delta\Psi_{\alpha-1}^\beta\rangle\|$. From Eq. (S.26), the first and second terms are bounded above by $(\alpha -$

$1/N_\alpha^2 \exp(-\beta^2 \Delta_g^2/2) \|H'\|^2 \Delta_g^{-1}$. For the third and fourth terms, by the mean value theorem, there exists a $\lambda \in (\lambda_{\alpha-1}, \lambda_\alpha)$ such that $E_\alpha - E_{\alpha-1} = \langle \Phi(\lambda) | H' | \Phi(\lambda) \rangle \Delta\lambda$. Because $|\langle \Phi(\lambda) | H' | \Phi(\lambda) \rangle| \leq \|H'\|$, the third and fourth terms have the same bound as the first and second terms, resulting in

$$\Delta\epsilon_\beta \langle \Psi_\alpha^\beta | \Psi_\alpha^\beta \rangle \leq \frac{4(\alpha-1)}{N_\alpha^2} e^{-\beta^2 \Delta_g^2/2} \frac{\|H'\|^2}{\Delta_g}, \quad (\text{S.40})$$

up to the leading order of $1/N_\alpha$. Since $\langle \Psi_\alpha^\beta | \Psi_\alpha^\beta \rangle \geq 1 - \eta$ and $\epsilon_\beta = \sum_{\alpha=1}^{N_\alpha} \Delta\epsilon_\beta$, we obtain

$$\epsilon_\beta \leq 2e^{-\beta^2 \Delta_g^2/2} \frac{\|H'\|^2}{\Delta_g} \frac{1}{1-\eta}. \quad (\text{S.41})$$

2. The trotterization errors

Following the same reasoning as in the previous discussion on β and from Eq. (S.37), we derive the bound for the error term $\Delta\epsilon_T \langle \Psi_\alpha^{\beta,T} | \Psi_\alpha^{\beta,T} \rangle$ as

$$\Delta\epsilon_T \langle \Psi_\alpha^{\beta,T} | \Psi_\alpha^{\beta,T} \rangle \leq 4 \frac{\alpha-1}{N_\alpha} \frac{\left(\sum_{\alpha'=1}^{N_\alpha} C_{\alpha',p}^{1/p} M_{1+p}^{1/p}(\beta) \right)^p}{(N_T/2)^p} \|H'\|, \quad (\text{S.42})$$

Summing over α , the total Trotterization error is

$$\epsilon_T = \sum_{\alpha=1}^{N_\alpha} \Delta\epsilon_T. \quad (\text{S.43})$$

Using the bound for $\Delta\epsilon_T$, we obtain

$$\epsilon_T \leq 2N_\alpha \left(\frac{N_T}{2} \right)^{-p} \left(\sum_{\alpha=1}^{N_\alpha} C_{\alpha,p}^{1/p} M_{1+p}^{1/p}(\beta) \right)^p \frac{\|H'\|}{1-\eta}. \quad (\text{S.44})$$

3. The sampling errors

Defining $g(\mathbf{t}) = (2\pi\beta^2)^{-\alpha} e^{-(t_1^2+t_2^2+\dots+t_{2\alpha}^2)/(2\beta^2)}$, we express

$$y(\mathbf{t}) = \langle \Phi_0 | e^{-iK_1 t_{2\alpha}} e^{-iK_2 t_{2\alpha-1}} \dots e^{-iK_\alpha t_\alpha} (H_\alpha - H_{\alpha-1}) e^{-iK_{\alpha-1} t_{\alpha-1}} e^{-iK_{\alpha-2} t_{\alpha-2}} \dots e^{-iK_1 t_1} | \Phi_0 \rangle, \quad (\text{S.45})$$

and

$$x(\mathbf{t}) = \langle \Phi_0 | e^{-iK_1 t_{2\alpha}} e^{-iK_2 t_{2\alpha-1}} \dots e^{-iK_\alpha t_\alpha} e^{-iK_{\alpha-1} t_{\alpha-1}} e^{-iK_{\alpha-2} t_{\alpha-2}} \dots e^{-iK_1 t_1} | \Phi_0 \rangle. \quad (\text{S.46})$$

The computation of Eq. (8) can then be viewed as finding the ratio of the expectation values of $y(\mathbf{t})$ and $x(\mathbf{t})$ under the probability distribution $g(\mathbf{t})$. Using N_ν samples, the averages \bar{x} and \bar{y} are estimators of $x(\mathbf{t})$ and $y(\mathbf{t})$, respectively, with \bar{y}/\bar{x} serving as the estimator for the energy difference.

Since each term in $y(\mathbf{t})$ is bounded by $\Delta\lambda \|H'\|$, we have $\|\bar{y}\| \leq \Delta\lambda \|H'\|$, $\sigma_y^2 \leq (\Delta\lambda)^2 \|H'\|^2$, and the variance of the estimator satisfies $\sigma_{\bar{y}}^2 \leq (\Delta\lambda)^2 \|H'\|^2 / N_\nu$. Similarly, for $x(\mathbf{t})$, $\sigma_x^2 \leq 1/N_\nu$. Using the delta method [29] and assuming independent sampling of \mathbf{t} for \bar{x} and \bar{y} , the variance of the ratio \bar{y}/\bar{x} is given by

$$\sigma_{\bar{y}/\bar{x}}^2 = \frac{1}{\bar{x}^2} \left(\sigma_{\bar{y}}^2 + \frac{\bar{y}^2}{\bar{x}^2} \sigma_{\bar{x}}^2 \right) \leq \frac{(\Delta\lambda)^2 \|H'\|^2}{N_\nu \bar{x}^2} \left(1 + \frac{1}{\bar{x}^2} \right). \quad (\text{S.47})$$

Thus, the standard error $\sigma_{E_\alpha - E_{\alpha-1}}$ for the energy difference computed using Eq. (S.1) satisfies

$$\sigma_{E_\alpha - E_{\alpha-1}} \leq \Delta\lambda \frac{\|H'\|}{\sqrt{N_\nu}} \frac{1}{\langle \Psi_\alpha^\beta | \Psi_\alpha^\beta \rangle} \sqrt{1 + \frac{1}{\langle \Psi_\alpha^\beta | \Psi_\alpha^\beta \rangle^2}}. \quad (\text{S.48})$$

The cumulative error for the energy estimation is then

$$\sigma_{E_\alpha} = \sigma_{E_\alpha - E_0} \leq \sum_{\alpha'=1}^{\alpha} \sigma_{E_{\alpha'} - E_{\alpha'-1}}. \quad (\text{S.49})$$

Using Eq. (S.48) and $\langle \Psi_\alpha^\beta | \Psi_\alpha^\beta \rangle \geq 1 - \eta$,

$$\sigma_{E_\alpha} \leq \frac{\alpha}{N_\alpha} \frac{\|H'\|}{\sqrt{N_\nu}} \frac{1}{1-\eta} \sqrt{1 + \frac{1}{(1-\eta)^2}}. \quad (\text{S.50})$$

Finally, by setting $\alpha = N_\alpha$ and $\epsilon_{mc} = \sigma_{E_\alpha}$, we obtain Eq. (21).

C. Error analysis and cost estimation for $\langle O \rangle$

In this section, we analyze error of $\langle O \rangle$ estimated from QZMC. The error of $\langle O \rangle$ is decomposed as $\epsilon_\beta + \epsilon_T + \epsilon_{mc}$, while, ϵ_β arises from the finite β , ϵ_T is due to trotterization, and ϵ_{mc} results from the finite number of samples.

1. The projection errors

From $|\Psi_\alpha^\beta\rangle = |\Psi_\alpha\rangle + |\delta\Psi_\alpha^\beta\rangle$, the expectation value $\langle \Psi_\alpha^\beta | O | \Psi_\alpha^\beta \rangle$ has an error given by

$$\delta \langle \Psi_\alpha^\beta | O | \Psi_\alpha^\beta \rangle = \langle \delta\Psi_\alpha^\beta | O | \Psi_\alpha \rangle + \langle \Psi_\alpha | O | \delta\Psi_\alpha^\beta \rangle + \langle \delta\Psi_\alpha^\beta | O | \delta\Psi_\alpha^\beta \rangle, \quad (\text{S.51})$$

which is bounded by

$$2\| |\delta\Psi_\alpha^\beta\rangle \| \|O\| + \| |\delta\Psi_\alpha^\beta\rangle \|^2 \|O\|. \quad (\text{S.52})$$

Considering errors up to the first order of $\| |\delta\Psi_\alpha^\beta\rangle \|$, we simplify the bound to

$$\delta \langle \Psi_\alpha^\beta | O | \Psi_\alpha^\beta \rangle \leq 2\| |\delta\Psi_\alpha^\beta\rangle \| \|O\|. \quad (\text{S.53})$$

The error ϵ_β in the expectation value $\langle \Psi_\alpha^\beta | O | \Psi_\alpha^\beta \rangle / \langle \Psi_\alpha^\beta | \Psi_\alpha^\beta \rangle$ is then estimated as

$$\delta \left(\frac{\langle \Psi_\alpha^\beta | O | \Psi_\alpha^\beta \rangle}{\langle \Psi_\alpha^\beta | \Psi_\alpha^\beta \rangle} \right) = \frac{\delta \langle \Psi_\alpha^\beta | O | \Psi_\alpha^\beta \rangle}{\langle \Psi_\alpha^\beta | \Psi_\alpha^\beta \rangle} + \frac{\langle \Psi_\alpha | O | \Psi_\alpha \rangle}{\langle \Psi_\alpha | \Psi_\alpha \rangle^2} \delta \langle \Psi_\alpha^\beta | \Psi_\alpha^\beta \rangle, \quad (\text{S.54})$$

$$\leq 4 \frac{\|\delta \Psi_\alpha^\beta\|}{\langle \Psi_\alpha | \Psi_\alpha \rangle} \|O\|,$$

where we used $\langle \Psi_\alpha | O | \Psi_\alpha \rangle / \langle \Psi_\alpha | \Psi_\alpha \rangle \leq \|O\|$. Using Eq. (S.26), this gives

$$\epsilon_\beta \leq 4 \|O\| e^{-\beta^2 \Delta_g^2 / 2} \|H'\| \Delta_g^{-1} (1 - \eta)^{-1}. \quad (\text{S.55})$$

To ensure the projection error remains smaller than ϵ_β , we require

$$\beta \geq \frac{1}{\Delta_g} \sqrt{2 \log \left(\frac{\|H'\| 4 \|O\|}{\Delta_g (1 - \eta) \epsilon_\beta} \right)}. \quad (\text{S.56})$$

2. The trotterization errors

The discussion of the Trotterization error follows a similar approach to that of the projection error. The key difference is that $|\delta \Psi_\alpha^\beta\rangle$ is replaced by $|\delta \Psi_\alpha^{\beta,T}\rangle$, and $\langle \Psi_\alpha | \Psi_\alpha \rangle$ is replaced by $\langle \Psi_\alpha^\beta | \Psi_\alpha^\beta \rangle$. Thus, the error ϵ_T in $\langle O \rangle$ is estimated as

$$\epsilon_T \leq 4 \frac{\|\delta \Psi_\alpha^{\beta,T}\|}{\langle \Psi_\alpha^\beta | \Psi_\alpha^\beta \rangle} \|O\|. \quad (\text{S.57})$$

Using Eq. (S.37), this becomes

$$\epsilon_T \leq 4 \frac{\|O\|}{1 - \eta} N_\alpha \left(\frac{N_T}{2} \right)^{-p} \left(\sum_{\alpha'=1}^{N_\alpha} C_{\alpha',p}^{1/p} M_{1+p}^{1/p}(\beta) \right)^p. \quad (\text{S.58})$$

The Trotterization error can be kept below ϵ_T by using the total trotter steps of

$$N_T \geq 2 \frac{(4N_\alpha \|O\|)^{1/p}}{(\epsilon_T (1 - \eta))^{1/p}} \sum_{\alpha=1}^{N_\alpha} C_{\alpha,p}^{1/p} \langle t^{1+p} \rangle_\beta^{1/p}. \quad (\text{S.59})$$

3. The sampling errors

The standard error $\sigma_{\langle O \rangle_\alpha}$ can be estimated using a similar approach as the standard error of E_α . This gives

$$\sigma_{\langle O \rangle_\alpha} \leq \frac{\|O\|}{\sqrt{N_\nu}} \frac{1}{1 - \eta} \sqrt{1 + \frac{1}{(1 - \eta)^2}}. \quad (\text{S.60})$$

To achieve $\sigma_{\langle O \rangle_\alpha} \leq \epsilon_{\text{mc}}$, the number of samples N_ν can be chosen as

$$N_\nu \geq \epsilon_{\text{mc}}^{-2} \|O\|^2 (1 - \eta)^{-2} (1 + (1 - \eta)^2). \quad (\text{S.61})$$

D. Remarks

1. Errors from inaccurate energies

In this discussion, we assume $\Delta_g \beta \geq 1$. This assumption is reasonable because the calculation becomes infeasible otherwise. If there is an energy error ϵ in E_α , the approximate projection operator is expressed as

$$P^\beta (H_\alpha - E_\alpha - \epsilon) = \sum_{m_\alpha} e^{-\beta^2 (\mathcal{E}_{m,\alpha} - E_\alpha - \epsilon)^2} |m_\alpha\rangle \langle m_\alpha|. \quad (\text{S.62})$$

If ϵ is comparable to Δ_g , the approximate projection operator can project onto states other than the target state. For $\epsilon \ll \Delta_g$, we analyze the difference:

$$\begin{aligned} & P^\beta (H_\alpha - E_\alpha - \epsilon) - e^{-\beta^2 \epsilon^2 / 2} P^\beta (H_\alpha - E_\alpha) \\ &= \sum_{m_\alpha \neq \Phi_\alpha} e^{-\beta^2 ((\mathcal{E}_{m,\alpha} - E_\alpha)^2 + \epsilon^2)} \\ & \quad \left[e^{-\beta^2 \epsilon (\mathcal{E}_{m,\alpha} - E_\alpha)} - 1 \right] |m_\alpha\rangle \langle m_\alpha|. \end{aligned} \quad (\text{S.63})$$

When $\Delta_g \beta \sim 1$, the term $[\exp(-\beta^2 \epsilon (\mathcal{E}_{m,\alpha} - E_\alpha)) - 1]$ becomes small because $\epsilon \ll \Delta_g$. When $\Delta_g \beta \gg 1$, the factor $\exp(-\beta^2 ((\mathcal{E}_{m,\alpha} - E_\alpha)^2 + \epsilon^2))$ becomes small. In either case, for $\epsilon \ll \Delta_g$,

$$P^\beta (H_\alpha - E_\alpha - \epsilon) \approx e^{-\beta^2 \epsilon^2 / 2} P^\beta (H_\alpha - E_\alpha). \quad (\text{S.64})$$

Consecutive application of Eq. (S.64) instead of $P^\beta (H_\alpha - E_\alpha)$ changes $|\Psi_\alpha^\beta\rangle$ to

$$e^{-\alpha \beta^2 \epsilon^2 / 2} |\Psi_\alpha^\beta\rangle. \quad (\text{S.65})$$

2. Quantum circuit implementation

This section illustrates several quantum circuits employed in the Quantum Zeno Monte Carlo (QZMC) method. Figure S.1 presents the QZMC circuits that uses controlled time-evolution. If the noise levels experienced by circuits (a) and (c) differ significantly, circuit (d) can be used instead of (a) to calculate $\langle \Psi | \Psi \rangle$, mitigating the influence of noise.

The circuits shown in Figure S.1 are general and applicable to any Hamiltonian. However, they can be highly susceptible to device noise due to the large number of controlled time-evolution operations. To address this limitation, the circuits in Figure S.2 can be used. These circuits eliminate the need for controlled time-evolution if a common eigenstate $|\Phi_{\text{ref}}\rangle$ exists for H_1, \dots, H_{N_α} . Although this requirement may seem restrictive, many practical physical and chemical systems share a common eigenstate - the vacuum.

For Green's function calculations, it is necessary to compute g_α as defined in Eq. (S.10). Using Pauli string decomposition, this computation reduces to a weighted sum of terms such as

$$\begin{aligned} & \langle \Phi_0 | e^{-iH_1 t_{2\alpha+1}} e^{-iH_2 t_{2\alpha}} \dots e^{-iH_\alpha t_{\alpha+2}} P_{\gamma'} \\ & \quad e^{-iH_\alpha t_{\alpha+1}} P_\gamma e^{-iH_\alpha t_\alpha} \dots e^{-iH_1 t_1} | \Phi_0 \rangle, \end{aligned} \quad (\text{S.66})$$

where P_γ represents a Pauli string. This means that Green's function calculations can be performed using the quantum circuits shown in Figure S.3.

As noted in the method section of the main text, 1 and 2 qubit unitary matrix can be compressed to a circuit with a small number of gates. Figure. S.4 depict these compressed circuit.

III. ADDITIONAL DATA ON ONE AND TWO-QUBIT SYSTEMS

In this section, we give additional calculational data on one and two qubit systems considered in the main text.

A. One-Qubit System

In the main text, we analyzed a one-qubit system described by the Hamiltonian

$$H(\lambda) = \frac{X}{2} + (2\lambda - 1)Z, \quad (\text{S.67})$$

where λ traverses from 0 to 1 via a discrete path defined by $\lambda_\alpha = \alpha/N_\alpha$. In this section, we use a noiseless simulator to evaluate the parameter dependencies of QZMC by varying N_α and β , as well as to assess the impact of finite Trotterization steps.

Figure S.5 illustrates these dependencies for $\langle \Psi | \Psi \rangle$ and the ground-state energy E of $H(\lambda = 1)$. Figures S.5(a) and S.5(b) show the dependence on β , revealing increased accuracy with β up to $\beta = 10$. For $\beta > 10$, the factor $e^{-N_\alpha \beta^2 \epsilon^2}$ becomes too small, where ϵ refers to the error in the energy estimation, causing a significant reduction in $\langle \Psi_\alpha^\beta | \Psi_\alpha^\beta \rangle$, as discussed in the main text. This leads to large errors in the estimated energies, as seen in Fig. S.5(b).

Figures S.5(c) and S.5(d) demonstrate the variation of $\langle \Psi | \Psi \rangle$ and E with N_α , showing convergence to the exact values as N_α increases. Notably, E achieves accuracy as soon as $\langle \Psi | \Psi \rangle$ takes on a non-trivial value, around $N_\alpha = 5$.

Finally, Figures S.5(e) and S.5(f) present results with Trotterization. The Trotterized time evolution $U_\alpha(\tau, N_{T,\alpha})$ for H_α is defined as

$$U_\alpha(\tau, N_{T,\alpha}) = \prod_{l=1}^{N_{T,\alpha}} e^{-i\Delta\tau X/2} e^{-i\Delta\tau(2\lambda_\alpha - 1)Z}, \quad (\text{S.68})$$

where $\Delta\tau = \tau/N_{T,\alpha}$. We used the same $N_{T,\alpha}$ for all α , and the total number of Trotter steps N_T was calculated as $N_T = 2 \sum_{\alpha=1}^{N_\alpha} N_{T,\alpha}$. For instance, $N_T = 200$ corresponds to $N_{T,\alpha} = 10$ for each α .

With increasing N_T , $\langle \Psi | \Psi \rangle$ converges to its exact value, while E converges more rapidly. This indicates the resilience of E to inaccuracies in the time evolution caused by finite Trotterization steps.

B. Hubbard dimer

We demonstrate the application of QZMC to the Hubbard dimer using Trotterized time evolution on the *ibm perth* quantum computer. To simplify the analysis, we focus solely on the ground state and employ second-order Trotterization for the time evolution. For $H = H_1 + H_2$, the second-order Trotterized time evolution $U(\tau, n_T)$ is defined as

$$U(\tau, n_T) = \prod_{l=1}^{n_T} e^{-i\Delta\tau H_1/2} e^{-i\Delta\tau H_2} e^{-i\Delta\tau H_1/2}, \quad (\text{S.69})$$

where $\Delta\tau = \tau/n_T$.

For Figures S.6(a) and S.6(b), we used the compressed circuit described in Fig. S.4(b). The Trotterization was performed using Eq. (S.69) with $N_{T,\alpha} = n_T = 4$ for each α , $H_1 = -\frac{U}{2}(I + Z_1 Z_2)$, and $H_2 = -t(X_1 + X_2)$. These results demonstrate the robustness of our algorithm in the presence of both Trotterization errors and device noise.

However, circuit compression is not always feasible. To address this, we tested our algorithm with an uncompressed implementation of the Trotterization, which notably increased the circuit depth and reduced $\langle \Psi | \Psi \rangle$ compared to the compressed version.

To manage the increased depth, we employed QZMC with a reference state, as depicted in Fig. S.2. The reference state used is $|\Psi_{\text{ref}}\rangle = [1/\sqrt{2} \ 0 \ 0 \ -1/\sqrt{2}]^T$, representing the first excited state of the Hamiltonian. Figures S.6(c) and S.6(d) show results with $N_\alpha = 4$ and $N_{T,\alpha} = 1$ for each α .

We averaged two different Trotterization choices: one with $H_2 = -\frac{U}{2}(I + Z_1 Z_2)$ and the other with $H_2 = -t(X_1 + X_2)$, as the choice significantly influences computational results when the number of Trotter steps is 1. Using the circuit in Fig. S.2(d), QZMC provided accurate energy values despite a reduction in $\langle \Psi | \Psi \rangle$.

The circuits used for QZMC with uncompressed Trotterization are shown in Fig. S.7. Figure S.7(a) represents the initialization circuit, while Fig. S.7(c) mimics the noise of the controlled-ZZ operation depicted in Fig. S.7(b).

IV. QUANTUM CIRCUIT FOR XXZ MODEL

As noted in the method section of the main text, we start with the ground state $|\Phi_0\rangle$ of

$$H_0 = -J \sum_{i:\text{odd}} (S_i^x S_{i+1}^x + S_i^y S_{i+1}^y + \Delta S_i^z S_{i+1}^z). \quad (\text{S.70})$$

The initialization circuit that prepares the vacuum state $|0^n\rangle$ when the ancilla qubit is in $|0\rangle$ and $|\Phi_0\rangle$ when the ancilla qubit is in $|1\rangle$ is depicted in Fig. S.8.

V. ADDITIONAL DATA ON NOISELESS SIMULATIONS

Here, we provide additional data on the noiseless simulations in Figures 5-6 of the main text, along with the quantum

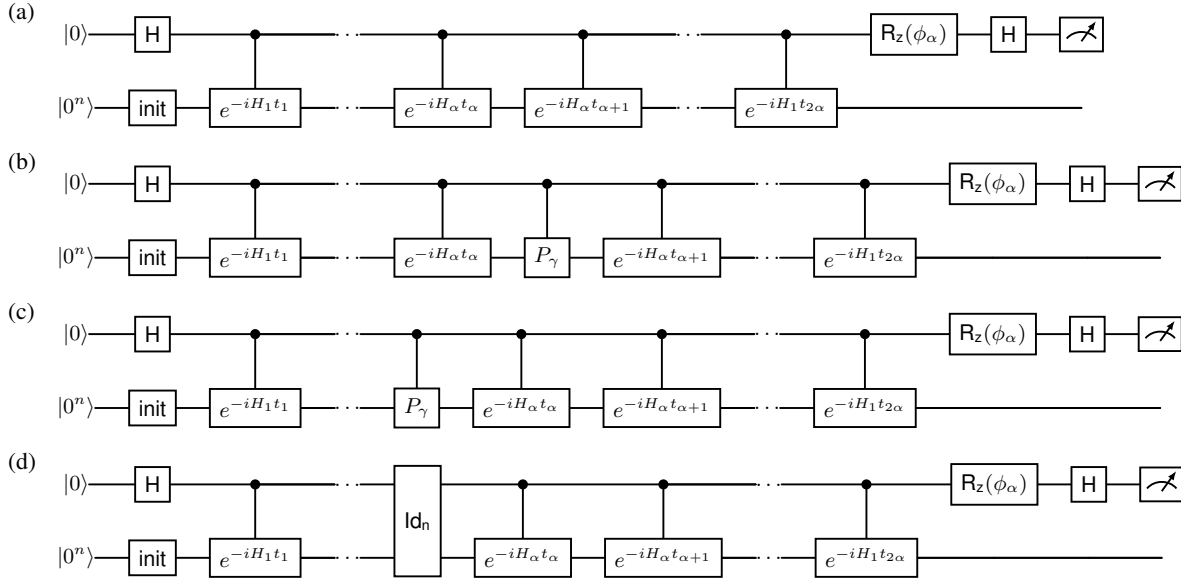


Figure S.1. **Quantum circuits for QZMC without a reference state.** (a) Circuit for $\langle \Psi_\alpha | \Psi_\alpha \rangle$. (b) Circuit for $\langle \Psi_\alpha | O | \Psi_\alpha \rangle$. (c) Circuit for $\langle \Psi_\alpha | \Phi_\alpha \rangle \langle \Phi_\alpha | (H_\alpha - H_{\alpha-1}) | \Psi_{\alpha-1} \rangle$. The noise difference between $\langle \Psi_\alpha | \Psi_\alpha \rangle$ and $\langle \Psi_\alpha | \Phi_\alpha \rangle \langle \Phi_\alpha | (H_\alpha - H_{\alpha-1}) | \Psi_{\alpha-1} \rangle$ can be mitigated by using circuit (d), which includes a noisy identity operation that mimics the noise effect of controlled- P_γ , instead of circuit (a). The circuit $\boxed{\text{init}}$ refers to the transformation of $|0^n\rangle$ into $|\Phi_0\rangle$. Here, $\phi_\alpha = \sum_{\alpha'=1}^{\alpha} E_{\alpha'}(t_{\alpha'} + t_{2\alpha+1-\alpha'})$

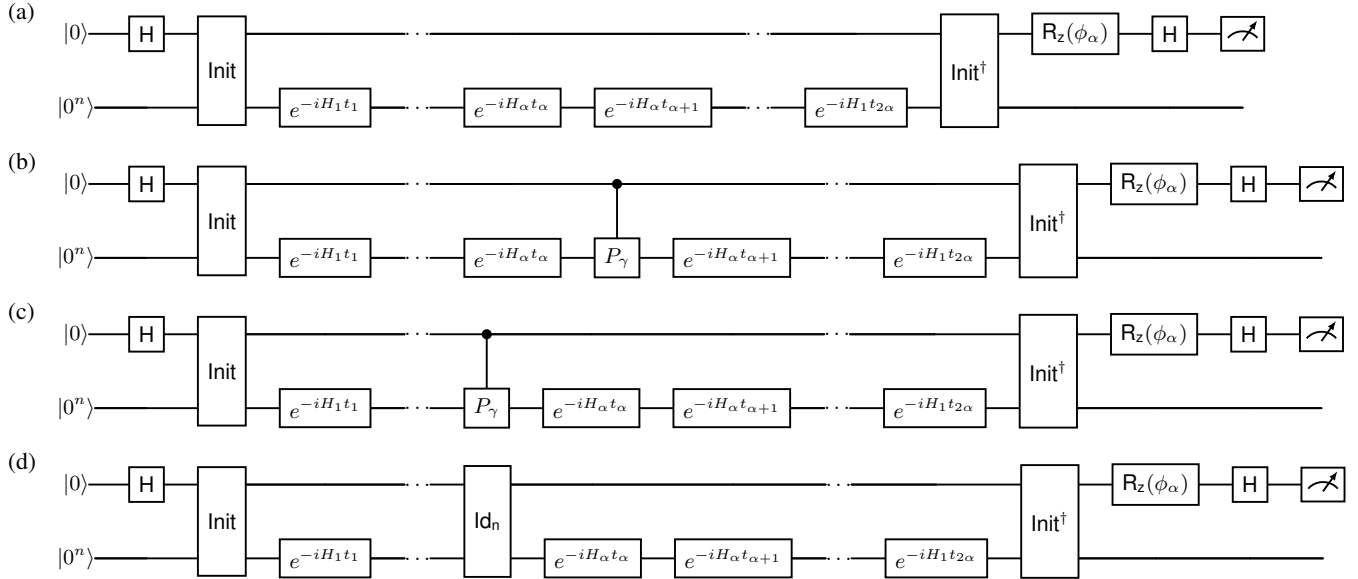


Figure S.2. **Quantum circuits for QZMC with a reference state.** (a) Circuit for $\langle \Psi_\alpha | \Psi_\alpha \rangle$. (b) Circuit for $\langle \Psi_\alpha | O | \Psi_\alpha \rangle$. (c) Circuit for $\langle \Psi_\alpha | \Phi_\alpha \rangle \langle \Phi_\alpha | (H_\alpha - H_{\alpha-1}) | \Psi_{\alpha-1} \rangle$. (d) Circuit for $\langle \Psi_\alpha | \Psi_\alpha \rangle$, including a noisy identity operation $\boxed{Id_n}$, which makes the noise effect on $\langle \Psi_\alpha | \Psi_\alpha \rangle$ and $\langle \Psi_\alpha | \Phi_\alpha \rangle \langle \Phi_\alpha | (H_\alpha - H_{\alpha-1}) | \Psi_{\alpha-1} \rangle$ similar. The circuit $\boxed{\text{init}}$ transforms $|0^n\rangle$ into a reference state $|\Phi_{\text{ref}}\rangle$ when the control qubit is in $|0\rangle$, and into $|\Phi_0\rangle$ when the control qubit is in $|1\rangle$. And the phase ϕ_α is equal to $\sum_{\alpha'=1}^{\alpha} E_{\alpha'}(t_{\alpha'} + t_{2\alpha+1-\alpha'})$

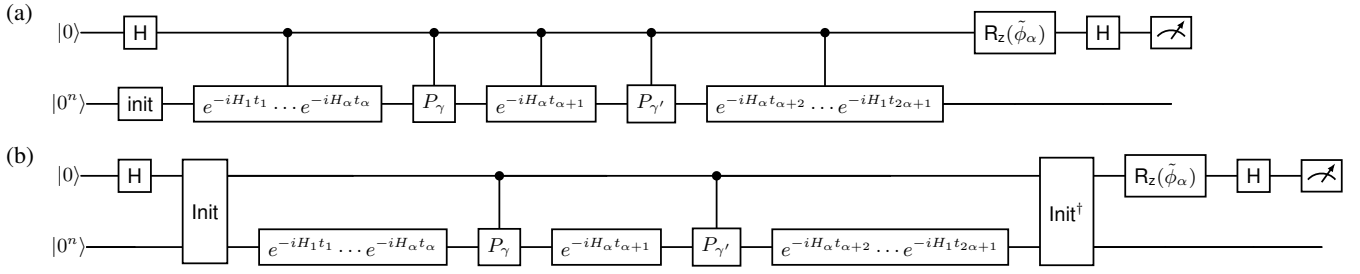


Figure S.3. **Quantum circuits for Green's function.** (a) Circuit without a reference state. (b) Circuit with a reference state. For the phase $\tilde{\phi}_\alpha$, $\tilde{\phi}_\alpha = \phi_\alpha = \sum_{\alpha'=1}^{\alpha} E_{\alpha'}(t_{\alpha'} + t_{2\alpha+2-\alpha'}) + (E + \omega)t_{\alpha+1}$ for the real part, and $\tilde{\phi}_\alpha = \phi_\alpha - \pi/2$ for the imaginary part.

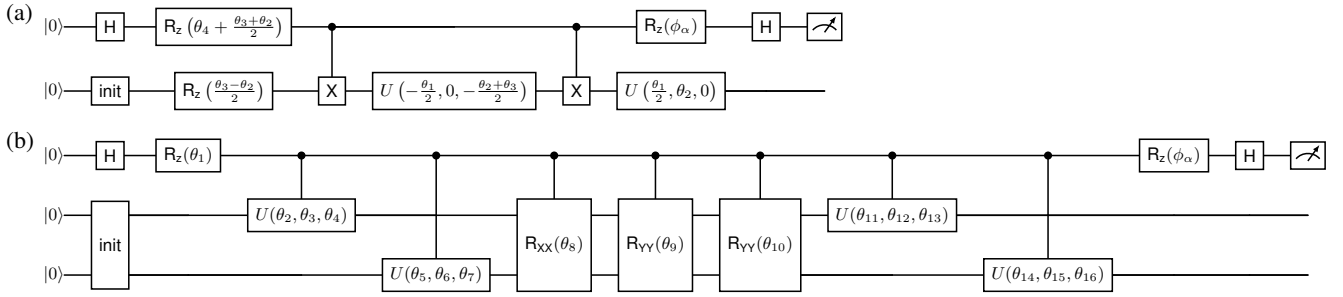


Figure S.4. **Quantum circuits for QZMC using 1- and 2-qubit circuit compression.** (a) Compressed circuit for 1-qubit systems. (b) Compressed circuit for 2-qubit systems.

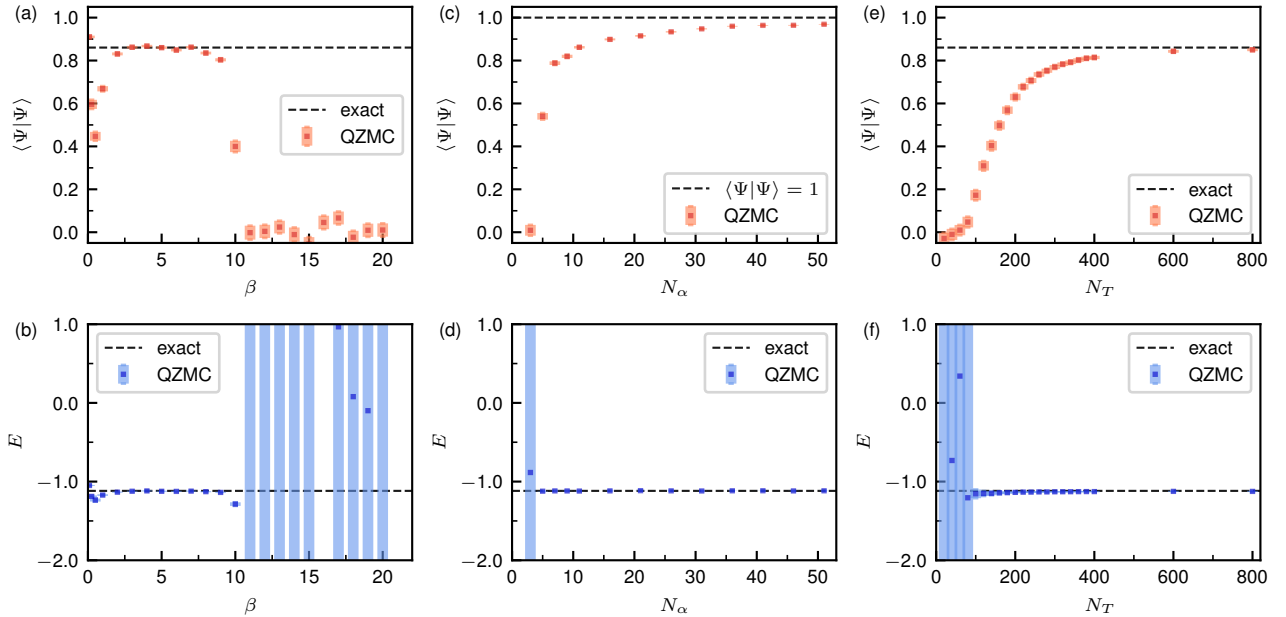


Figure S.5. **Parameter dependence of QZMC applied to the one-qubit system.** (a) and (b) illustrate the dependence of $\langle \Psi | \Psi \rangle$ and E on β , respectively, with $N_\alpha = 10$ and exact time evolution. (c) and (d) demonstrate how $\langle \Psi | \Psi \rangle$ and E vary with N_α , using $\beta = 5$ and exact time evolution. (e) and (f) plots dependence of $\langle \Psi | \Psi \rangle$ and E on N_T , with $\beta = 5$ and $N_\alpha = 10$. Squares represent data points, while shaded regions indicate numerically estimated error bars. In this figure, we used $N_\nu = 400$.

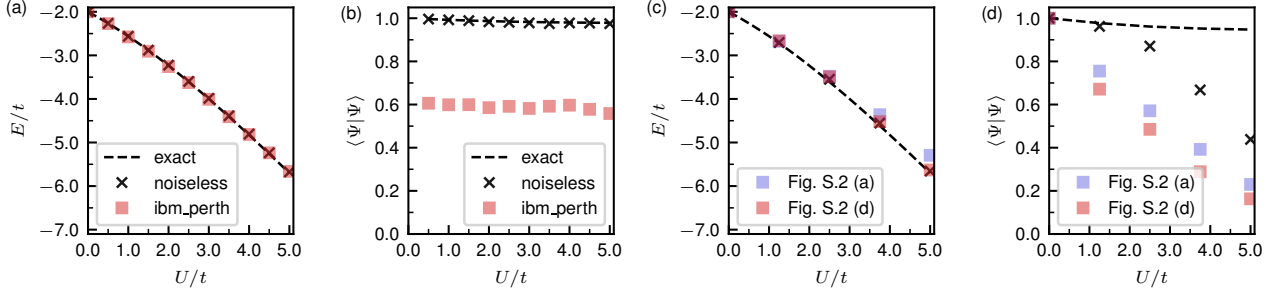


Figure S.6. **QZMC for the Hubbard dimer with Trotterized time evolution.** (a) and (b) show results using the compressed circuit (Fig. S.4(b)) with four Trotter steps for each time evolution. (c) and (d) present results with uncompressed Trotterized time evolutions with one Trotter step for each time evolution. In (c) and (d), red squares represent calculations performed with the circuit in Fig. S.2(d), while blue squares correspond to Fig. S.2(a). In this figure, squares indicate results obtained using *ibm_perth*, black crosses represent noiseless simulations, and dotted lines denote the exact results. All calculations were performed with $\beta = 0.5$ and $N_\nu = 100$.

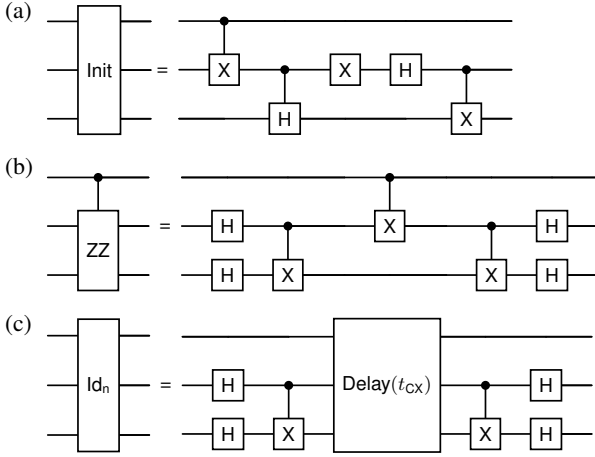


Figure S.7. **Quantum circuits for the Hubbard dimer.** (a) initialization circuit for the Hubbard dimer that prepare $|\Phi_0\rangle$ if the ancilla (topmost) qubit is at $|1\rangle$ and $|\Phi_{\text{ref}}\rangle$ if the ancilla qubit is at $|0\rangle$. (b) Implementation of the controlled-ZZ operation. (c) Noisy identity circuit used to mimic errors induced by the controlled-ZZ operation. In (c), t_{CX} represents the duration of the CNOT operation, and $\text{Delay}(t)$ indicates the system waiting for a duration of t .

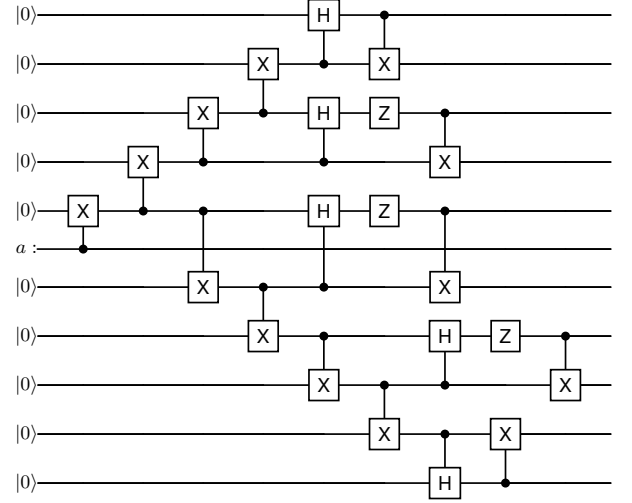


Figure S.8. **Quantum circuits for the XXZ model.** This figure shows the initialization circuit for the 10-site XXZ model. The qubit labeled "a" represents the ancilla qubit used to compute the overlap.

circuit in Figure S.9 that implements Eq. (33), the ground state of the Hubbard dimer.

Figure S.10(a)-(f) depicts $\langle \Psi | \Psi \rangle$ for Hubbard models studied in Fig. 5. These figures illustrate that increasing N_α in proportion to the number of sites yields consistent values of $\langle \Psi | \Psi \rangle$ across the different Hubbard models. For comparison, we also plotted $\langle \Psi | \Psi \rangle$ without Trotterization. All figures indicate that the Trotterization error significantly affects $\langle \Psi | \Psi \rangle$. In most cases, the Trotterization error is the dominant source of deviation in $\langle \Psi | \Psi \rangle$, except for the 2×4 Hubbard model, where the first-order perturbation energy becomes inaccurate near $\lambda = 0.7 - 0.8$. Figures S.10(g) and (h) present spectral functions calculated using QZMC for 6-site Hubbard models.

Moreover, specific values of N_ν and total Trotter steps $N_T = 2 \sum_{\alpha=1}^{N_\alpha} N_{T,\alpha}$ for each model in Fig. 5 are summarized

Table S.1. N_ν , N_T , # of gates used for Fig. 5

Model	N_ν	N_T	# of gates
6×1	576	528	1.63×10^6
8×1	1024	930	5.19×10^6
10×1	1600	1444	1.28×10^7
2×3	933	726	1.97×10^6
2×4	1660	1268	6.02×10^6
2×5	2594	1960	1.45×10^7

in Table S.1.

Next, we give a comparison of Trotterization dependence for our method and the adiabatic state preparation (ASP) in Fig. S.11. For the comparison, we used a linearly interpolated Hamiltonian for ASP, $H_j = H_0(1 - j\Delta t/T_{\text{ASP}}) + H_j j\Delta t/T_{\text{ASP}}$

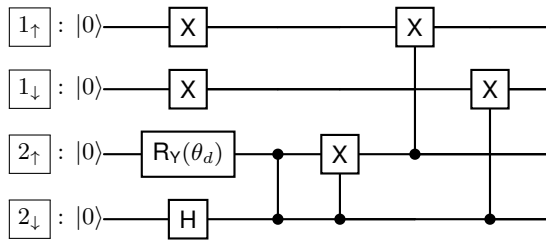


Figure S.9. **Quantum circuit for the ground state of the Hubbard dimer.** The quantum circuit used to prepare the ground state of the Hubbard dimer is shown. The parameter θ_d is defined in Eq. (34).

and tested several choices of Δt in Fig. S.11 (a). Then, where QZMC and ASP (without Trotterization) yield similar accuracy and maximum evolution times ($\Delta t = 0.5$ and $T_{\text{ASP}} = 9$ for ASP and $\beta = 1.5$, $N_\alpha = 4$ for QZMC), we computed the ground-state energy error as a function of the number of Trotterization steps. The results clearly show that QZMC converges much faster than ASP.

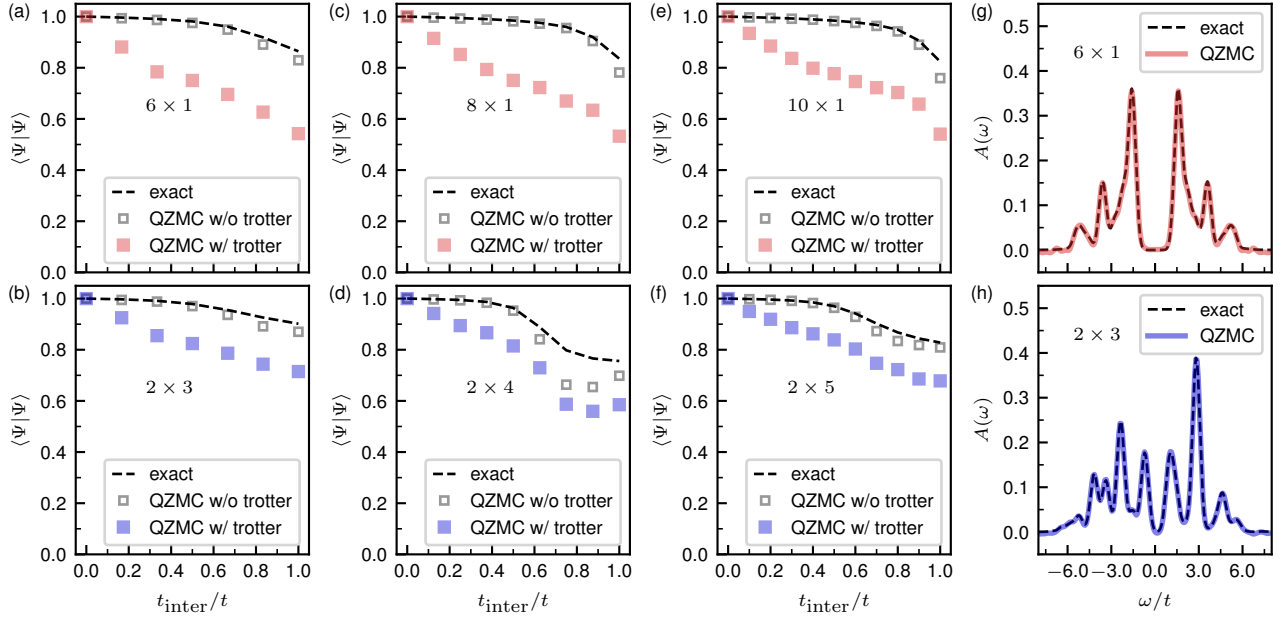


Figure S.10. **The half-filled Hubbard model in various sizes with QZMC.** (a)-(f) show $\langle \Psi | \Psi \rangle$ for Hubbard models of various sizes. (g) and (h) present the spectral function for the 6-site Hubbard model.

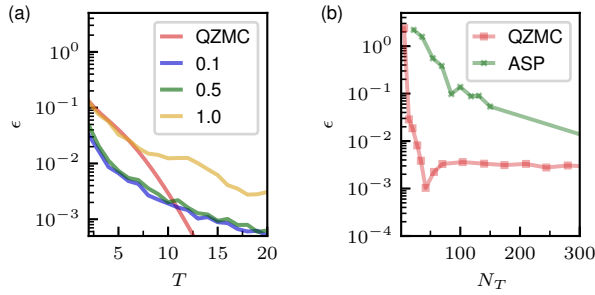


Figure S.11. **Comparison of QZMC and ASP** The ground-state energy estimation error ϵ is shown as a function of the maximum time length T for QZMC (red) and ASP with $\Delta t = 0.1, 0.5, 1.0$ (blue, green, and yellow) in (a). In (b), ϵ is plotted as a function of the number of Trotter steps N_T . The system considered is a 4×1 Hubbard model at half-filling with $U/t = 4$ under open boundary conditions and the initial Hamiltonian H_0 is a collection of dimers. In this figure, both ASP and QZMC start with $|\Phi_0\rangle$, the ground state of H_0 . For QZMC, we used $N_\alpha = 4$ and $N_\nu = 16, 384$.